

1
2
3
4
5
6
7
8
9
10
11
12
13
14
15
16
17
18
19
20
21

This version of the article has been revised based on one round of peer review and was last updated on 1 July 2022. It was subsequently resubmitted to *Basin Research* and has now been accepted. The accepted manuscript is available at <https://doi.org/10.1111/bre.12698>. Please note that the published version of record may contain different content from this preprint.

Inverting passive margin stratigraphy for marine sediment transport dynamics over geologic time

Charles M. Shobe^{1,2}, Jean Braun^{2,3}, Xiaoping Yuan^{2,4}, Benjamin Campforts^{2,5}, Boris Gailleton², Guillaume Baby^{6,7}, François Guillocheau⁶, and Cécile Robin⁶

¹*Department of Geology and Geography, West Virginia University, Morgantown, WV, USA*

²*Helmholtz Centre Potsdam, GFZ German Research Centre for Geosciences, Potsdam, Germany*

³*Institute of Geosciences, University of Potsdam, Potsdam, Germany*

⁴*Hubei Key Laboratory of Critical Zone Evolution, School of Earth Sciences, China University of Geosciences, Wuhan, China*

⁵*Community Surface Dynamics Modeling System, Boulder, CO, USA*

⁶*Géosciences Rennes, Université de Rennes, CNRS, UMR 6118, 35000 Rennes, France*

⁷*Physical Science and Engineering Division, King Abdullah University of Science and Technology, Thuwal, Saudi Arabia*

CMS (*corresponding author): charles.shobe@mail.wvu.edu

JB: jb Braun@gfz-potsdam.de

XY: xyuan@gfz-potsdam.de

BC: benjamin.campforts@colorado.edu

BG: boris.gailleton@gfz-potsdam.de

GB: baby.guillaume@gmail.com

FG: francois.guillocheau@univ-rennes1.fr

CR: cecile.robin@univ-rennes1.fr

30 **Inverting passive margin stratigraphy for marine sediment**
31 **transport dynamics over geologic time**

32 **Charles M. Shobe^{1,2,*}, Jean Braun^{2,3}, Xiaoping Yuan^{2,4}, Benjamin Campforts^{2,5}, Boris**
33 **Gailleton², Guillaume Baby^{6,7}, François Guillocheau⁶, and Cécile Robin⁶**

34 *¹Department of Geology and Geography, West Virginia University, Morgantown, WV, USA*

35 *²Helmholtz Centre Potsdam, GFZ German Research Centre for Geosciences, Potsdam, Germany*

36 *³Institute of Geosciences, University of Potsdam, Potsdam, Germany*

37 *⁴Hubei Key Laboratory of Critical Zone Evolution, School of Earth Sciences, China University*
38 *of Geosciences, Wuhan, China*

39 *⁵Community Surface Dynamics Modeling System, Boulder, CO, USA*

40 *⁶Géosciences Rennes, Université de Rennes, CNRS, UMR 6118, 35000 Rennes, France*

41 *⁷Physical Science and Engineering Division, King Abdullah University of Science and*
42 *Technology, Thuwal, Saudi Arabia*

43

44 *Corresponding author: Charles M. Shobe. Email: charles.shobe@mail.wvu.edu. Mail: 330
45 Brooks Hall, 98 Beechurst Ave., Morgantown, WV 26506.

46

47 **HIGHLIGHTS**

- 48 • We compare two, 2-D stratigraphic forward models against observed marine stratigraphy.
- 49 • One model uses purely local transport dynamics while one incorporates nonlocal
- 50 transport.
- 51 • The model incorporating nonlocal transport processes produces the better fit to the data.

- 52 • Nonlocal, momentum-driven transport processes produce diagnostic stratigraphy.
- 53 • Inferring past terrestrial landscape dynamics from stratigraphy may require nonlocal
- 54 models.

55

56 **ABSTRACT**

57 Passive margin stratigraphy contains time-integrated records of landscapes that have long
58 since vanished. Quantitatively reading the stratigraphic record using coupled landscape evolution
59 and stratigraphic forward models (SFMs) is a promising approach to extracting information
60 about landscape history. However, there is no consensus about the optimal form of simple SFMs
61 because there has been a lack of direct tests against observed stratigraphy in well constrained test
62 cases. Specifically, the extent to which SFM behavior over geologic space and time scales should
63 be governed by local (downslope sediment flux depends only on local slope) versus nonlocal
64 (sediment flux depends on factors other than local slope, such as the history of slopes
65 experienced along a transport pathway) processes is currently unclear. Here we develop a
66 nonlocal, nonlinear SFM that incorporates slope bypass and long-distance sediment transport,
67 both of which have been previously identified as important model components but not
68 thoroughly tested. Our model collapses to the local, linear model under certain parameterizations
69 such that best-fit parameter values can indicate optimal model structure. Comparing 2-D
70 implementations of both models against seven detailed seismic sections from the Southeast
71 Atlantic Margin, we invert the stratigraphic data for best-fit model parameter values and
72 demonstrate that best-fit parameterizations are not compatible with the local, linear diffusion
73 model. Fitting observed stratigraphy requires parameter values consistent with important
74 contributions from slope bypass and long-distance transport processes. The nonlocal, nonlinear

75 model yields improved fits to the data regardless of whether the model is compared against only
76 the modern bathymetric surface or the full set of seismic reflectors identified in the data. Results
77 suggest that processes of sediment bypass and long-distance transport are required to model
78 realistic passive margin stratigraphy, and are therefore important to consider when inverting the
79 stratigraphic record to infer past perturbations to source regions.

80

81 **INTRODUCTION**

82 Reconstructing landscape evolution trajectories—and the environmental boundary conditions
83 that governed them—from the geologic past is a key goal in geomorphology. Such
84 reconstructions are challenging because erosion processes continually destroy past topography,
85 leaving only minor traces of ancient landscapes (e.g., river terraces; Molnar et al., 1994; Schanz
86 et al., 2018; Yuan et al., 2022) from which to deduce past landscape boundary conditions.
87 Fortunately, every source has its sink; all sediment eroded from a terrestrial drainage basin must
88 go somewhere. The sedimentary record, in regions where it is preserved and where there exists
89 plausible long-term connectivity between source and sink, therefore represents our best hope of
90 inferring time-resolved records of landscape change and its tectonic and climatic drivers with
91 reasonable accuracy and precision. One geologic setting with particularly high potential for the
92 preservation of relatively complete records of terrestrial erosion is marine passive margin basins,
93 which contain Earth's most complete archives of sediment sourced from adjacent, eroding
94 terrestrial environments (e.g., Steckler et al., 1988; Allen and Allen, 2013).

95 Passive margin stratigraphy can, under the right conditions, be used to reconstruct past
96 tectonic and climatic perturbations to Earth's surface (e.g., Poag and Sevon, 1989; Poag, 1992;
97 Pazzaglia and Brandon, 1996; Baby et al., 2018; Ding et al., 2019a). While the stratigraphic

98 record can suffer from signal buffering, stratigraphic incompleteness, and signal shredding (e.g.,
99 Sadler, 1981; Jerolmack and Paola, 2010; Straub et al., 2020), the variability that leads to these
100 effects is thought to yield average behavior that can be predicted at passive margin evolution
101 timescales (tens to hundreds of Ma). Passive margin stratigraphy may reflect large-scale, long-
102 lasting perturbations to landscapes provided that those perturbations have amplitudes and
103 durations that exceed the background level of “noise” in the sedimentary system (Straub et al.,
104 2020). Historically, efforts to read the stratigraphic record of passive margins have focused on
105 the study of sediment thickness, volume, texture, lithological/mineralogical makeup, and
106 chemistry, yielding interpretations about past terrestrial erosion dynamics (e.g., Poag and Sevon,
107 1989). As numerical stratigraphic forward models (SFMs) became more common (e.g., Steckler
108 et al., 1993; 1996; Syvitski and Hutton, 2001; Granjeon and Joseph, 1999; Burgess et al., 2006;
109 Burgess, 2012), stratigraphic modelers began to use inverse techniques to extract environmental
110 forcing information from forward simulation of the stratigraphic record (e.g., Lessenger and
111 Cross, 1996; Cross and Lessenger, 1999; Bornholdt and Westphal, 1998; Bornholdt et al., 1999;
112 Imhof and Sharma, 2006; 2007; Olivene et al., 2014; Zhang et al., 2021). The great potential of
113 that record for revealing past landscape evolution has led to efforts to couple landscape evolution
114 models (LEMs) and SFMs (e.g., Granjeon and Joseph, 1999; Salles and Hardiman, 2016; Salles
115 et al., 2018; Ding et al., 2019a,b; Yuan et al., 2019a, Salles, 2019; Zhang et al., 2020) to build
116 full source-to-sink models, and in some cases to use large ensembles of those models to directly
117 invert observed stratigraphy for terrestrial erosion dynamics (e.g., Yuan et al., 2019a). The idea
118 underpinning such inversions is that misfit between observed and modeled stratigraphy can be
119 minimized to reveal best-fit values for relevant forcing parameters such as rock uplift rate,

120 assuming that the model is an accurate representation of erosion, transport, and deposition
121 processes integrated over geologic time.

122 Many previous efforts focused on margin spatial scales and ~100 Ma timescales have used an
123 approach in which marine sediment transport is conceptualized as being linearly dependent on
124 local bathymetric slope, which when combined with mass conservation yields a linear-diffusion-
125 like model (e.g., Moretti and Turcotte, 1985; Kenyon and Turcotte, 1985; Rivenaes, 1992; 1997;
126 Ross et al., 1994; Paola, 2000; Braun et al., 2013; Rouby et al., 2013; Yuan et al., 2019a; Zhang
127 et al., 2020). However, this approach might not be capable of producing large-scale stratal
128 geometries that agree with observations. In the stratigraphy of many passive margin basins, we
129 observe substantial accumulations of sediment hundreds of kilometers from shore on the
130 continental rise and abyssal plain that must have bypassed the higher-gradient continental slope
131 (Lowe, 1976; Syvitski et al., 1988) and then been transported long distances over negligible
132 slopes on the basin floor (Wynn et al., 2002; Talling et al., 2012, Luchi et al., 2018; Hereema et
133 al., 2020).

134 The sole dependence of sediment flux on local slope neglects both sediment transport over
135 very low slopes and the potential influence of nonlocal transport processes, or those processes
136 for which the distribution of sediment travel distances is heavy-tailed such that some sediment
137 moves long distances relative to the scale of the model grid (e.g., Fofoula-Georgiou et al.,
138 2010). Transport processes are especially likely to deviate from local-slope-dependent behavior
139 when sediment particles are fine enough to be suspended in the water column as observed in
140 turbidity currents and other marine mass flows (e.g., Parker et al., 1986; Mohrig et al., 1998). In
141 a nonlocal conceptualization of downslope sediment transport, erosion or deposition at a point
142 has some dependence on surface slope elsewhere (Furbish and Roering, 2013; Doane et al.,

143 2018). Nonlocal processes like sediment plumes from river mouths, turbidity currents, marine
144 landslides, and debris flows are responsible for much of the long-distance transport observed
145 along passive margins and are therefore relevant for any model that seeks to simulate passive
146 margin stratigraphy. Such processes and deposits may not be fully consistent with the
147 assumptions or predictions of local, linear transport models because they may require nonlocal
148 and/or nonlinear conceptualizations of sediment transport dynamics.

149 Stratigraphic forward modeling studies have moved beyond local, linear diffusion models to
150 incorporate nonlocal sediment transport dynamics with varying degrees of complexity (e.g.,
151 Granjeon and Joseph, 1999; Syvitski and Hutton, 2001; Sømme et al., 2009; Granjeon, 2014;
152 Harris et al., 2016; Ding et al., 2019a, Falivene et al., 2019). However, the extent to which
153 nonlocality should play a role in large-scale SFMs remains unclear, as previous comparisons
154 between local and nonlocal transport formulations have not always revealed clear differences
155 (Granjeon, 2014), and few studies have focused on the deep, distal portions of margins where
156 nonlocal process dynamics may contribute most to shaping margin form. While substantial effort
157 has been devoted to parameterizing large-scale terrestrial landscape evolution models (e.g.,
158 Guerit et al., 2019; Yanites et al., 2018; Barnhart et al., 2019; Barnhart et al., 2020a,b,c) to test
159 how well they predict landscape form (e.g., van der Beek and Bishop, 2003; Valla et al., 2010;
160 DiBiase and Whipple, 2011; Hobbey et al., 2011; Barnhart et al., 2020b), the same is not true of
161 SFMs. The mathematical form of simple, long-term/large-scale seascape evolution models that
162 best represents the development of passive margin stratigraphy is currently an open question.

163 Here we test a generalized two-dimensional (2-D) SFM that moves beyond local, linear
164 diffusion by incorporating, as suggested by previous work, sediment transport dynamics that
165 allow sediment to bypass steep slopes and travel beyond the base of the continental slope. Our

166 approach is intended not to simulate such processes explicitly, but to model their integrated
167 effects over geologic time. We test the relative applicability of this nonlocal model and the local,
168 linear model by quantitative comparison against seismic stratigraphic data from well-studied
169 passive margin basins along the Southeast Atlantic Margin (SAM), southern Africa. Results from
170 model-data comparison indicate that, at least over ~100 Ma timescales, passive margin seascape
171 evolution and the development of marine stratigraphy are most consistent with a model that
172 incorporates nonlocal and nonlinear transport dynamics. This indicates that passive margin
173 evolution may be dominated by nonlocal, nonlinear sediment transport processes that may be
174 critical ingredients in models used to invert passive margin stratigraphy for past environmental
175 forcings.

176

177 **MODELING SEASCAPE EVOLUTION OVER GEOLOGIC TIME**

178

179 **Model Dimensionality**

180 Below, we cast the local, linear and nonlocal, nonlinear models in a form that, by
181 convention in the SFM literature (and in contrast to conventions governing LEMs), is referred to
182 as 2-D because any point in the model grid can be uniquely specified by a horizontal and a
183 vertical coordinate. This choice is essential to keep our model evaluation exercise tractable and
184 interpretable given the available stratigraphic data, but it is important to note that fully 3-D SFMs
185 are routinely used (e.g., Falivene et al., 2020; Zhang et al., 2021) and in some cases allow
186 development of preferential nonlocal sediment transport pathways (e.g., submarine canyons) that
187 the models we test here can only claim to represent on average over geologic time (e.g.,
188 Granjeon, 2014).

189

190 **The Local, Linear Diffusion Model**

191 The simplest and longest-standing approach to modeling seascape evolution (and therefore
192 the way, by tracking the bathymetric surface through time, of modeling marine stratigraphy) is to
193 use an analogy to the heat equation that yields a linear diffusion equation where elevation z is the
194 variable “diffusing” over time and where the gradient driving diffusion is the bathymetric slope
195 $\frac{\partial z}{\partial x}$ (Kenyon and Turcotte, 1985; Ross et al., 1994). The downslope sediment flux per unit contour
196 length q_s goes linearly with local slope ($S = \frac{\partial z}{\partial x}$ for simplicity):

$$197 \quad q_s = -K_d S, \quad (1)$$

198 and the divergence of sediment flux sets the rate of bathymetric change:

$$199 \quad \frac{\partial z}{\partial t} = -\frac{\partial q_s}{\partial x} = K_d \frac{\partial^2 z}{\partial x^2}. \quad (2)$$

200 Here K_d [L^2/T] is a transport coefficient that governs the rate of bathymetric diffusion. The key
201 assumption in this approach is that downslope sediment flux goes linearly with the local slope,
202 such that no variables beyond K_d and bathymetry influence the rate of seascape evolution.

203 There is no clear physical basis for such a slope-dependent diffusion equation at low slopes
204 (i.e., on the continental shelf) and shallow water depths (see Paola, 2000 for a review), and an *ad*
205 *hoc* solution has been to assert that the diffusion rate constant declines with water depth d (e.g.,
206 Kaufman et al., 1992; van Balen et al., 1995) as wave- and storm-driven bed shear stresses are
207 reduced:

$$208 \quad K_d(d) = K_{d_0} e^{-d/d_*}. \quad (3)$$

209 Here K_{d_0} is the diffusion rate constant at the water surface ($d = 0$) and d_* is the e-folding depth
210 scale that governs the decline in K_d with depth below the water surface. When d_* is small

211 relative to the total basin depth (i.e., when there are substantial declines in sediment transport
212 efficiency with depth), the linear diffusion approach yields morphologies analogous to
213 continental shelves, shelf breaks, and steeper continental slopes. Similar results are achieved by
214 asserting that terrestrial sediment fluxes deposit at a fixed slope when they reach the shoreline
215 and then become subject to marine sediment transport by linear diffusion (Yuan et al., 2019a).
216 Linear diffusion models, with or without modifications in the shallow environment, deliver little
217 sediment beyond the base of the continental slope because the governing equation asserts that the
218 downslope sediment flux approaches zero as the local slope approaches zero.

219 The inconsistency of local, linear diffusion models with observations of nonlocal transport
220 and long-distance sedimentation has long been noted (e.g., Syvitski et al., 1988), and has
221 motivated model modifications such as adding advective components of sediment transport
222 (Niedoroda et al., 1995; Pirmez et al., 1998; Thran et al., 2020), allowing sediment bypass on
223 slopes above some angle (e.g., Lowe, 1976; Syvitski et al., 1988; Ross et al., 1994; Thran et al.,
224 2020), and enforcing that only some (potentially slope-dependent) proportion of the sediment
225 flux may be deposited at any given point, with the rest being routed downslope (Ding et al.,
226 2019a, Thran et al., 2020). There are also several higher-complexity, 3-D SFMs that incorporate
227 nonlocal transport by explicitly simulating advective processes (e.g., Granjeon and Joseph, 1999;
228 Granjeon, 2014; Falivene et al., 2019). Here we generalize ideas from existing SFMs, as well as
229 recent advances from terrestrial landscape evolution modeling, into a simple SFM that
230 incorporates two key modifications to account for both transport over low slopes and nonlocal
231 transport.

232 **A Modified Seascape Evolution Model**

233 The modified model is a generalization of existing ideas for how seascape evolution
234 might deviate from the local, linear model that (1) is simple enough to be applied over basin-
235 filling timescales, (2) is parsimonious enough to allow iterative calibration of all parameters, and
236 (3) collapses under certain parameter values to the local, linear model. The model is most
237 intuitively cast in terms of a balance between the volumetric entrainment rate per unit bed area E
238 and volumetric deposition rate per unit bed area D (e.g., Beaumont et al., 1992; Kooi and
239 Beaumont, 1994; van Balen et al., 1995; Davy and Lague, 2009; Carretier et al., 2016; Shobe et
240 al., 2017; Yuan et al., 2019b; Campforts et al., 2020; Braun, 2021). The statement of mass
241 conservation that governs the change in bathymetry at a point is:

$$242 \quad \frac{\partial z}{\partial t} = -E + D . (4)$$

243 This framework is convenient because both of the models we propose to compare—the
244 local, linear model and the nonlocal, nonlinear model—can be represented by altering the
245 functional forms of E and D . As shown by Carretier et al. (2016), assuming that the entrainment
246 rate is linearly proportional to the local slope S :

$$247 \quad E = K_e S , (5)$$

248 that K_e is an entrainment rate constant [L/T], and that the deposition rate is the volumetric
249 sediment flux per unit width q_s over the model grid cell spacing dx :

$$250 \quad D = \frac{q_s}{dx} , (6)$$

251 yields the local, linear model with behavior identical to equation 2. Its two key assumptions are
252 that sediment entrainment depends only on local slope and that the deposition rate depends only
253 on the downslope sediment flux.

254 The nonlocal, nonlinear model uses equation 5 to calculate sediment entrainment but
255 makes two key modifications to equation 6 inspired by observations from passive margin

256 depositional systems. These are intended to allow (1) a nonlinear dependence of sediment
257 transport on local slope to account for the transition to mass failures and turbidity currents at
258 higher slopes as well as sediment bypass on slopes unable to sustain further steepening beyond
259 some critical slope at which frequent failures are generated, and (2) transport of sediment over
260 negligible slopes as observed in data from deep marine deposits (e.g., Wynn et al., 2002). Our
261 modified model rests heavily on recent advances in terrestrial and marine modeling, especially
262 the framework proposed by Carretier et al. (2016) for hillslope sediment transport.

263 Carretier et al. (2016) proposed altering equation 6 to encapsulate a nonlinear dependence
264 of the deposition rate on slope such that sediment deposition declines as slope increases towards
265 some imposed threshold (e.g., Andrews and Bucknam, 1987; Roering et al., 1999), such that:

$$266 \quad D = \frac{q_s \left(1 - \left(\frac{S}{S_c}\right)^2\right)}{dx}. \quad (7)$$

267 Here S_c is the critical slope, best thought of physically as the slope at or above which no further
268 deposition can occur and all remaining sediment continues downslope. As discussed by Carretier
269 et al. (2016), this model is nonlocal in the sense that sediment supplied from upslope can
270 continue downslope if the deposition rate is insufficient to disentrain all sediment. Similar
271 approaches to sediment bypass have also been used in recent seascape evolution models (e.g.,
272 Thran et al., 2020).

273 Equation 7 has one feature that makes it less than suitable for modeling marine transport:
274 at a slope of zero, all sediment in transport is deposited. This is not a problem encountered in the
275 eroding hillslopes for which the model was developed (Carretier et al., 2016), but contradicts the
276 observed behavior of marine sediment transport processes like turbidity currents that can travel
277 hundreds of km over negligible slopes. Because our goal is to simulate the integrated effects of

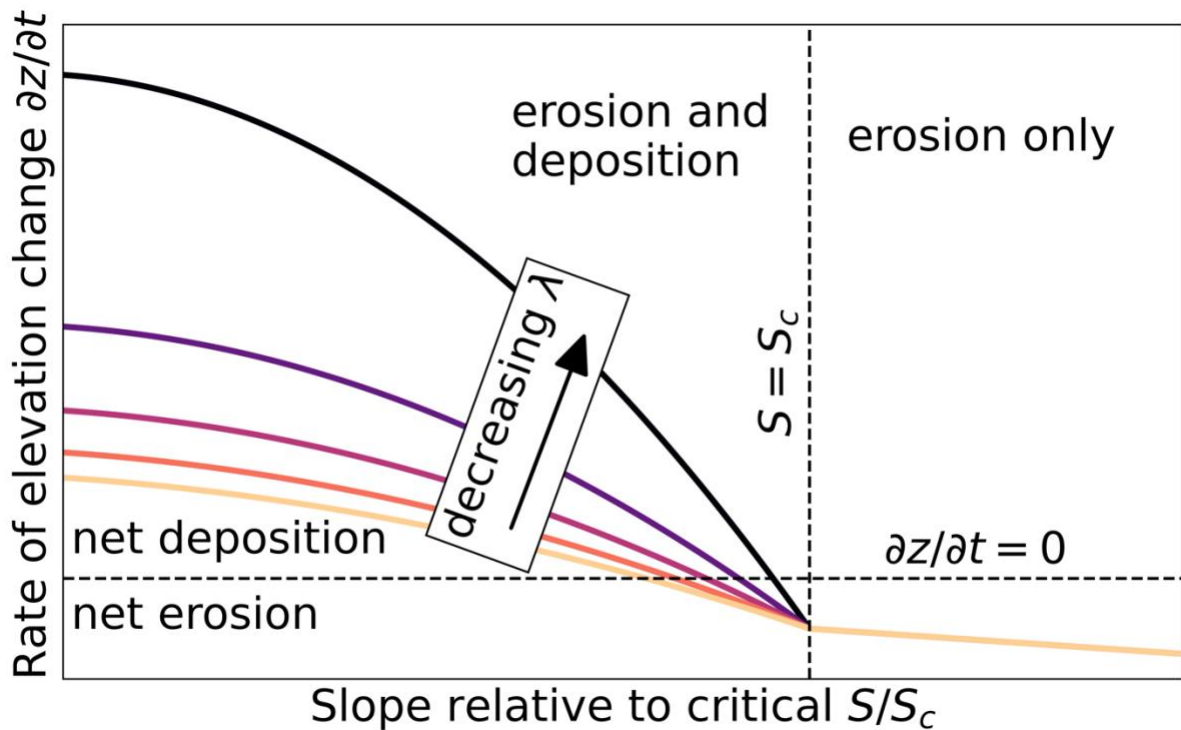
278 such events over basin-filling timescales, our model must have a mechanism for transport of
279 sediment over negligible slopes.

280 To allow transport of sediment over near-zero slopes, we modify Carretier et al's (2016)
281 model by adopting from Ding et al. (2019a) the idea that only some proportion of sediment in
282 transport will be deposited at any given location. We incorporate this modification by altering
283 equation 7 to:

$$284 \quad D = \frac{q_s \left(1 - \left(\frac{s}{s_c}\right)^2\right)}{\lambda}, \quad (8)$$

285 where λ is a sediment transport length scale that is at least the model grid cell spacing. When
286 $\lambda \gg dx$, only some small proportion of the amount of sediment in transport is deposited. The
287 rest continues in transport towards the distal portion of the margin. When $\lambda = dx$, all sediment in
288 transport is deposited. While this approach is heuristic—values of λ likely depend on grain size
289 but are not tied explicitly in our model to specific properties of the sediment or the transport
290 system—it allows the model to incorporate the general sediment transport patterns thought to
291 occur in the deep, distal portions of continental margins. Modeled sediment can travel long
292 distances down the continental slope because entrainment is linearly proportional to slope
293 (equation 5) and because deposition becomes negligible as slopes approach the critical slope of
294 non-deposition (equation 8). At the base of the continental slope, low slopes drive reduced
295 sediment entrainment rates and increased deposition rates, but the condition $\lambda \gg dx$ allows
296 continued transport across the abyssal plain in lieu of direct calculations of debris flow/turbidity
297 current transport (e.g., Parker et al., 1986). The modified model allows an approximation of
298 nonlocal transport in the sense that the amount of sediment deposited at a given distance from
299 shore depends not only on the local slope at that point but on all the points upslope that have
300 contributed sediment to—or removed it from—active transport.

301 At a point, the rate of elevation change responds to the sediment flux per unit width q_s ,
 302 the entrainment coefficient K_e , the slope S relative to the critical slope of non-deposition S_c , and
 303 the sediment transport length scale λ (Figure 1). For a given λ , there is a shift from net
 304 deposition to net erosion as S approaches S_c as the deposition rate declines and the entrainment
 305 rate increases. At a given S/S_c increasing λ causes a shift towards less deposition (or more net
 306 entrainment) as more sediment remains in transport. The S/S_c at which there exists a shift from
 307 net deposition to net entrainment (i.e., a shift from positive $\frac{\partial z}{\partial t}$ to negative $\frac{\partial z}{\partial t}$) depends on λ . For
 308 $S/S_c > 1$, no deposition can occur, λ ceases to matter, and entrainment continues to scale
 309 linearly with slope.



310
 311 **Figure 1: Model behavior—as shown by the rate of elevation change—as a function of $\frac{S}{S_c}$ (where $S = \frac{\partial z}{\partial x}$) and**
 312 **λ . Decreasing the transport length scale leads to increased deposition, and therefore positive changes in**
 313 **elevation, when the slope is below the slope of non-deposition. When the slope is at or above the slope of non-**
 314 **deposition, the transport length scale ceases to matter because no deposition occurs and all sediment bypasses**
 315 **the cell. The sediment entrainment rate increases linearly with slope, and deposition rate decreases**

316 **nonlinearly with slope, leading to net erosion as slopes increase towards the slope of non-deposition. The**
317 **erosion coefficient is held constant in this figure.**

318

319 We follow previous work (Kaufman et al., 1992; van Balen et al., 1995) in our treatment of

320 both the local, linear model and the nonlocal, nonlinear model by asserting that the erosion

321 coefficient K_e declines exponentially with water depth d below some surface value K_{e_0} :

322
$$K_e(d) = K_{e_0} e^{-d/d_*}. \quad (9)$$

323 This accounts for the erosive energy that may prevent the development of steep slopes close

324 to the shoreline. The complete governing equation for the commonly used linear, local model in

325 the erosion-deposition framework is found by substituting equations 5, 6, and 9 into equation 4:

326
$$\frac{\partial z}{\partial t} = -K_{e_0} e^{-d/d_*} S + \frac{q_s}{dx}. \quad (10)$$

327 The complete equation for bathymetric evolution under the nonlocal, nonlinear model is found

328 by substituting equations 5, 8, and 9 into equation 4:

329
$$\frac{\partial z}{\partial t} = -K_{e_0} e^{-d/d_*} S + \frac{q_s \left(1 - \left(\frac{S}{S_c}\right)^2\right)}{\lambda}. \quad (11)$$

330 Equation 10 has two parameters: the sediment entrainment coefficient at zero water depth

331 K_{e_0} [L/T] and the depth scale d_* [L] over which the entrainment coefficient declines with depth.

332 Equation 11 has two additional parameters: the slope of non-deposition S_c [-] and the sediment

333 transport length scale λ [L]. Sediment compaction due to the deposition of overburden is

334 calculated using the assumption of an exponential decay in porosity φ with depth below the

335 bathymetric surface h (e.g., Sclater and Christie, 1980; Yuan et al., 2019a):

336
$$\varphi(h) = \varphi_0 e^{-h/h_*}, \quad (12)$$

337 where φ_0 is the surface porosity and h_* is the e-folding length scale governing the decay of

338 porosity with depth. We used φ_0 and h_* values of 0.56 and 2830 m, respectively, obtained by

339 averaging the sand and clay compaction parameters of Guillocheau et al. (2012).

340 We only apply equation 11 to positive slopes (defined as sloping from the shore towards
341 the basin). For adverse slopes, we assert for simplicity that $E = 0$ and $D = \frac{q_s}{dx}$. The formulation
342 for adverse slopes would be important in environments where they occur more commonly, but
343 initial tests indicated minimal influence in our simulations where most slopes tilt towards the
344 basin floor.

345

346 **Conditions for the Collapse of the Nonlocal, Nonlinear Model to the Linear, Local Model**

347 The nonlocal, nonlinear model (equation 11) is convenient because it collapses to the local,
348 linear model (equation 10) under certain parameter values such that the key differences between
349 the two approaches can be undone with parameter changes alone. When the slope of non-
350 deposition S_c is infinitely large, or in practice is many times greater than the greatest slopes in
351 the model domain, there is no slope-driven reduction in the deposition rate and therefore no
352 sediment bypass on steep slopes. Similarly, when the sediment transport length scale λ is equal
353 to the model grid spacing dx (this corresponds physically to a case in which sediment cannot
354 travel far over near-zero slopes), there is no transport over flat regions. Parameter values in this
355 model are therefore a direct proxy for model structure (e.g., Barnhart et al., 2020a), meaning that
356 finding parameterizations that match observations can determine optimal model structure and
357 yield insight into seascape evolution processes.

358

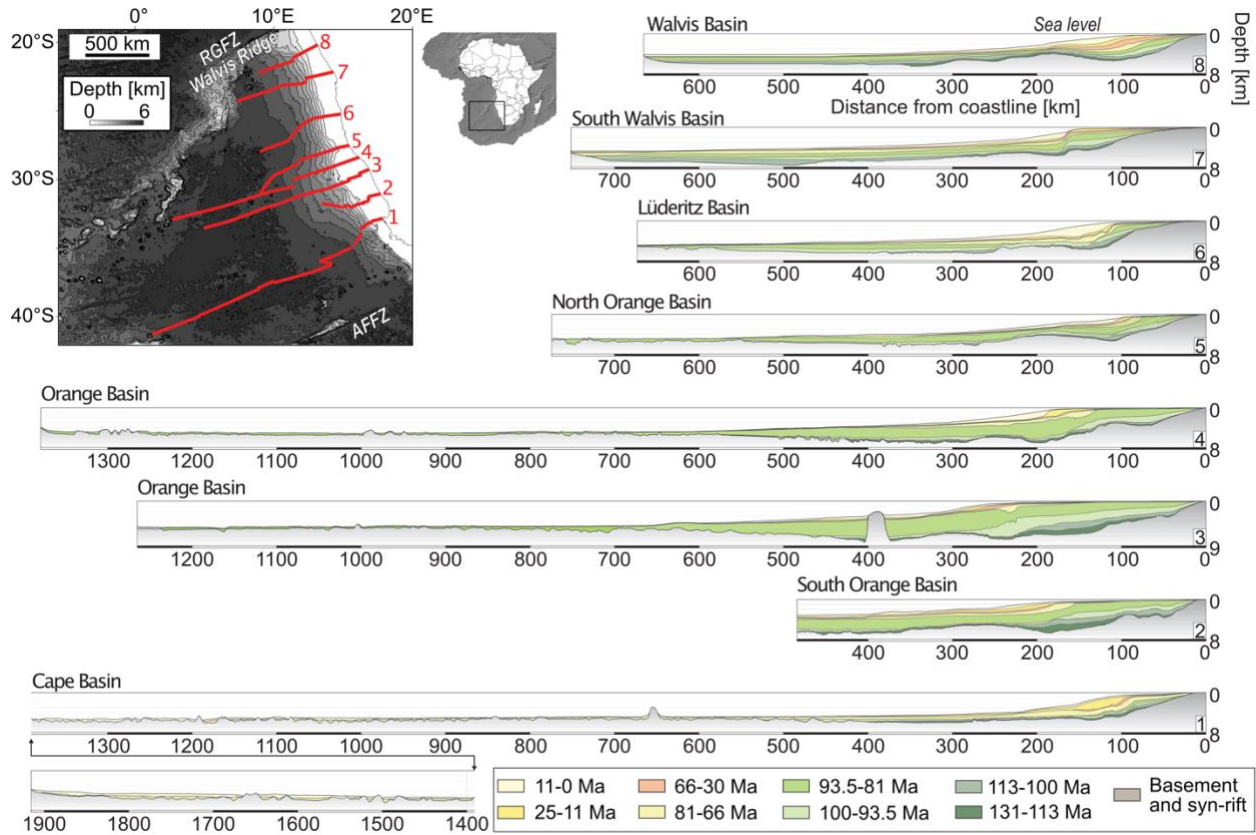
359 **METHOD FOR INVERSION OF PASSIVE MARGIN STRATIGRAPHY**

360 Our goal, rather than simulating margin evolution under an assumed set of parameter
361 values, is to develop insight into model structure by using a data-driven inversion to find the
362 parameter values that yield the best match between modeled and measured passive margin

363 stratigraphy. Best-fit parameter values will illuminate whether the deviations from the linear
364 diffusion approach encoded within our model (sediment bypass and long-distance transport) are
365 necessary to match observed stratigraphy.

366 **Study Area: the Southeast Atlantic Margin, Southern Africa**

367 The SAM is a well-studied passive margin sedimentary basin off the western coast of
368 southern Namibia and South Africa (Figure 2). Our study area consists of the Cape, Orange,
369 Lüderitz, and Walvis basins, which are bounded on the southeast by the Agulhas fracture zone
370 and on the northwest by the Rio Grande fracture zone. The basins were initially formed by early
371 Cretaceous rifting that opened the South Atlantic Ocean as Africa separated from South America
372 (e.g., Hirsch et al., 2010). Rifting initiated at ca. 250 Ma (Hirsch et al., 2010), but we focus only
373 on post-rift stratigraphy (Guillocheau et al., 2012; Baby et al., 2018; 2019). The earliest post-rift
374 units are dated to ca. 131 Ma (Baby et al., 2018). We selected the SAM because of the large
375 number of long (in terms of distance from the shoreline) seismic sections that have been
376 collected and interpreted (Guillocheau et al., 2012; Baby et al., 2018; 2019). Sections that have
377 continuous coverage from the shoreline to the nearly flat basin floor—typically reached at a
378 distance of between 300 and 600 km from shore on the SAM—are essential to constraining the
379 extent to which the long-distance sediment transport dynamics in our model adequately describe
380 the development of passive margin stratigraphy.



381
 382 **Figure 2: Study area and seismic data, modified from Baby et al. (2019). We use sections 1 and 3-8 and retain**
 383 **the section numbers from Baby et al. (2019) for clarity. We do not use section 2 for our parameter estimation**
 384 **experiments because the thickness of deposits beyond 500 km from the shoreline is unknown. RGFZ is the**
 385 **Rio Grande Fracture Zone; AFFZ is the Agulhas-Falkland Fracture Zone.**

386
 387 Seven seismic sections interpreted by Baby et al. (2018; 2019) comprise the dataset that
 388 we will use to test the two models and determine optimal model structure and parameter values
 389 (Figure 2). We omit one of their sections—their section 2 (Figure 2)—from our analysis because
 390 it is by far the shortest (< 500 km) and because at its end point there are deposits approximately 3
 391 km thick. It is not possible to evaluate models for long-distance sediment transport using section
 392 2 because the section ends before deposits reach a negligible thickness.

393 The data that is most easily compared to SFM output is the geometry of seismic
 394 reflectors. We use as our benchmark data sections that have been converted from two-way travel
 395 time to depth. Each section has nine seismic reflectors of interest, each representing the top of a
 396 particular unit as defined by Baby et al. (2019). The first (deepest) reflector of interest is the

397 contact between basement/syn-rift deposits and the first post-rift deposits, interpreted by Baby et
398 al. (2019) to occur at ca. 131 Ma. The ninth (uppermost) reflector is the modern bathymetric
399 surface. Because the basement/syn-rift surface will be manipulated as a model boundary
400 condition, there remain eight reflectors that can be used for model-data comparison when
401 determining best-fit model structure and parameter values.

402 **Inversion Methodology**

403 The procedure of our data-driven inversion approach—more formally classified as a
404 parameter inference exercise using a genetic algorithm—is to run successive “generations” (sets
405 of realizations) of the model that are run in parallel and then compared against data using a misfit
406 function we define below in the “Inversion Experimental Setup” section. The first generation
407 uses parameter values randomly drawn from a uniform distribution. Each generation yields a
408 subset of model runs with acceptable fits; a new generation of model realizations is then created
409 by randomly perturbing the parameter values (in our case using a Gaussian perturbation kernel
410 (Klinger et al., 2018)) of the runs from the previous generation that were deemed acceptable. By
411 running successive generations of realizations, the inversion procedure converges on a region of
412 the parameter space that yields best-fit parameter values. Because parameter values represent the
413 contributions of slope bypass and long-distance transport processes, best-fit parameter values
414 reveal the importance, or lack thereof, of those processes to passive margin evolution. For our
415 inversions we used the ABC-SMC (approximate Bayesian computation—sequential Monte
416 Carlo) algorithm implemented in PyABC (Klinger et al., 2018), an open-source Python package
417 that allows efficient parameter estimation using the iterative procedure described above. See
418 Sisson et al. (2007) and Toni et al. (2009) for details of ABC-SMC approaches, and Table S1 for
419 algorithm parameters used in our study.

420 There are many choices that govern inversion behavior, including the choice of the algorithm
421 itself. Our chosen approach is purposefully similar to genetic algorithm methods used in prior
422 efforts to infer parameters of SFMs (e.g., Lessenger and Cross, 1996; Bornholdt and Westphal,
423 1998; Bornholdt et al., 1999; Cross and Lessenger, 1999; Imhof and Sharma, 2006; 2007;
424 Falivene et al., 2014; Yuan et al., 2019a), but differs in the details of how successful
425 parameterizations are selected from each generation and perturbed to produce the next.
426 Exploratory testing of different parameter inference algorithm choices did not lead to
427 meaningfully different results.

428 Conducting such an inversion exercise requires estimating or assuming initial and boundary
429 conditions for the model that cannot be precisely known from geophysical and stratigraphic data
430 (for example, the subsidence history of the basin floor over the past 130 Ma). We also need to
431 define how model-data misfit will be calculated.

432 ***Model Setup and Initial and Boundary Conditions***

433 All model simulations run from 130 Ma, the approximate beginning of the post-rift
434 evolution of the SAM, to present day, with a timestep of 1,000 years. Model grid resolution is 10
435 km, a large spatial discretization but one commonly used in large-scale basin modeling (e.g.,
436 Granjeon, 2014) and that is sufficient to resolve the first-order morphology of the margin.
437 Because our goal is to invert for best-fit model parameters, rather than boundary conditions, we
438 must assume a set of boundary conditions lest we introduce too many variables into the
439 inversion. Assessment of inversion sensitivity to boundary conditions is a critical next step, but is
440 not treated here. The two key boundary conditions, both of which are functions of time, are the
441 geometry of the basement/syn-rift layer and the sediment flux to the modeled basin.

442 **Basement geometry.** The model is supplied with a value for basement elevation at every
443 point, both initially and at every subsequent timestep. We set initial basement geometry at 130
444 Ma by assuming that the initial post-rift basement had approximately 1/3 the depth, relative to a
445 steady datum, of the modern basement. We then assume that the basement subsided at an
446 exponentially declining rate (McKenzie, 1978) between 130 Ma and present, such that the
447 basement elevation over time at any point declines from its initial elevation to its known present
448 elevation, rapidly at first and then more slowly (with an e-folding time scale held constant at
449 23.67 Ma for all sections). These simplistic assumptions are broadly consistent with expectations
450 derived from simple thermal subsidence models (e.g., McKenzie, 1978) and give time series of
451 basement elevations in agreement with those deduced from basin reconstruction studies from the
452 Orange Basin (Hirsch et al., 2010). We do not model flexural subsidence due to sediment and
453 water loading (except in the sense that the deepest portions of the basement subside the fastest
454 from the initial to final condition) so that we can have consistent basement geometry between all
455 model runs for a given section to aid model comparison.

456 The other key simplification inherent to our treatment of basement geometry is that we do
457 not include any uplift or tilting of the margin over the course of its evolution. Stratigraphic
458 analysis (Rouby et al., 2009; Baby et al., 2018), thermochronologic measurements (Stanley et al.,
459 2021), basin modeling (Hirsch et al., 2010), and numerical modeling (Dauteuil et al., 2013;
460 Braun et al., 2014; Stanley et al., 2021) suggest that portions of the SAM experienced two
461 periods of rock uplift. The first was a pulse of tilting from ca. 81-66 Ma that affected the Orange
462 and Lüderitz basins and could have caused a maximum of 1,000 m of rock uplift in the proximal
463 portion of the margin (the distal portions of the margin, closer to the hinge point of the tilt, would
464 have experienced much less rock uplift; Aizawa et al., 2000; Paton et al., 2008; Hirsch et al.,

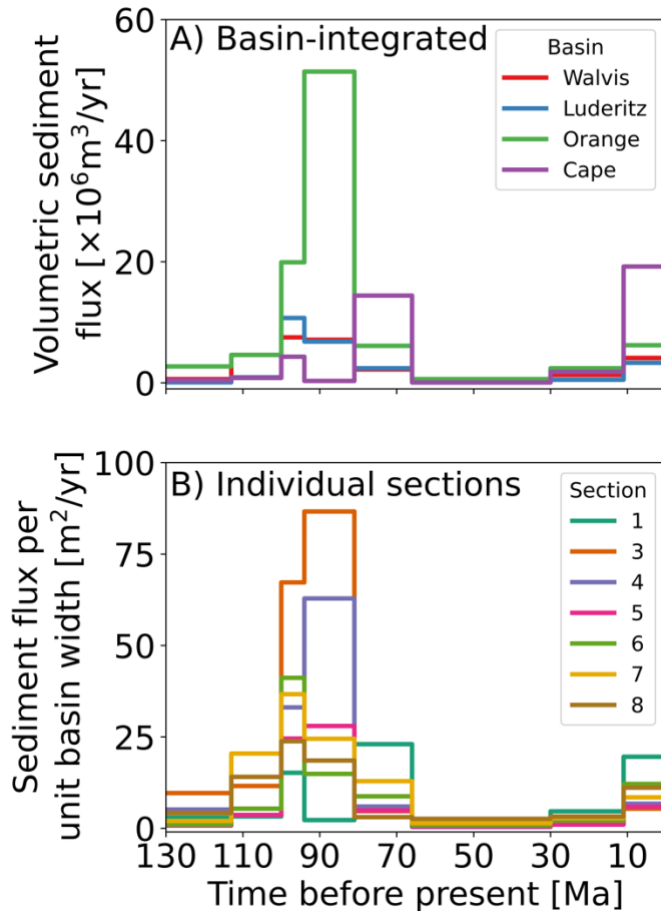
465 2010; Baby et al., 2018). This pulse is hypothesized to result from passage of Southern Africa
466 over a mantle superswell (Braun et al., 2014). The second hypothesized rock uplift pulse
467 occurred at ca. 30 Ma (though basin reconstruction studies report the pulse as occurring later at
468 ca. 16 Ma (Hirsch et al., 2010)) and had an amplitude of approximately 300-350 m (Baby et al.,
469 2018); the cause of this pulse remains unknown. We choose not to incorporate these
470 perturbations into our basement boundary condition. The magnitude and timing of uplift pulses
471 are inconsistent—and inconsistently constrained—among the four basins for which we have data
472 (Baby et al., 2018), and there is still debate about the existence and importance of the more
473 recent pulse (O'Malley et al., 2021). The magnitude of these perturbations is small relative to the
474 up to 7 km of deposits on the SAM. We acknowledge that incorporating these uplift pulses might
475 improve model-data misfit, but we argue that there is insufficient clarity in the data to
476 incorporate them, and that neglecting them would not lead to different conclusions with respect
477 to differentiating between the models we investigate.

478 ***Terrestrial sediment flux.*** The model requires a value for the terrestrial sediment flux
479 supplied to the basin at every timestep. Basin-scale sediment flux reconstructions for the SAM
480 rely on interpolation between seismic sections to derive estimates of volumetric sediment
481 delivery to the margin over the past 130 Ma (Guillocheau et al., 2012; Baby et al., 2019).
482 However, a cursory look at the sections of interest (Figure 2) shows that the total sediment
483 volume, as well as the volume during any given time interval, varies significantly among
484 sections within a given basin. To remove uncertainty surrounding the role of sediment flux, we
485 take the simplest possible approach: for each stratigraphic section to which we compare our
486 model, we calculate the sediment flux for each time period by integrating the volume of sediment
487 per unit margin width contained between each set of reflectors along each section while

488 accounting for post-deposition porosity loss due to compaction (see Shobe et al., 2022 for code).
489 This approach yields a total sediment volume per unit basin width [L^2] for each unit in each
490 section. Because the time duration represented by each section is known from previous work
491 (Guillocheau et al., 2012; Baby et al., 2018; 2019), we can then divide each unit's volume per
492 unit basin width by the time interval to get an average sediment flux to the section per unit width
493 per unit time [L^2/T]. Figure 3 shows the sediment flux time series obtained by integration, as
494 well as the basin-integrated sediment flux time series from Baby et al. (2019). The sediment flux
495 time series in any one section is reasonably similar to the basin-integrated sediment flux.
496 Estimates from our section integration approach are subject to uncertainty due to stratigraphic
497 incompleteness (e.g., Straub et al., 2020) caused by sediment moving into and out of the plane of
498 the section (i.e., parallel to the margin). There also are non-terrestrial sediments (i.e., carbonates
499 and pelagic deposits; Guillocheau et al., 2012; Baby et al., 2018) in our sections that are counted
500 as terrestrially derived sediment fluxes under our methodology. Incompleteness and non-
501 terrestrial sources likely introduce significant uncertainty into the terrestrial sediment flux
502 estimates. Given that the alternative to accepting these uncertainty sources is to assume that
503 reconstructed basin-scale sediment fluxes were evenly distributed among all sections in a given
504 basin, an idea not supported by section volumes or isopach maps (Baby et al., 2019), we argue
505 that we have made the safer assumption by conserving mass within each section we analyze to
506 enable direct comparison of modeled and measured seismic sections. Potential effects of
507 uncertainty in the sediment supply are worthy of future investigation.

508 **Sea level.** We hold sea level constant throughout all model experiments. The amplitude
509 of eustatic sea level variations (~120 m) is small relative to the length and depth scales of the
510 SAM both globally over the past 100 Ma (Bessin et al., 2017) and more recently throughout the

511 Quaternary off southern Africa specifically (Ramsay and Cooper, 2002). Further, the influence
512 of eustatic sea level on sediment delivery over geologic timescales to the deep, distal portions of
513 continental margins—the places where nonlocal transport dynamics may most influence
514 stratigraphy—is unclear (Sømme et al., 2009; Harris et al., 2016; 2018; 2020; Falivene et al.,
515 2020).



516

517 **Figure 3: (A) Volumetric fluxes of solid sediment from southern Africa to the four basins comprising the**
518 **SAM (Baby et al., 2019). These estimates were derived from interpolating between the sections shown in**
519 **Figure 3 (Guillocheau et al., 2012; Baby et al., 2018; 2019). (B) Volumetric solid sediment fluxes per unit**
520 **basin width derived in this study by integrating over the depth and length of each seismic section and**
521 **assuming an exponentially declining porosity profile. Given that the basins range from 500-1000 km wide, the**
522 **two estimates agree to an order of magnitude.**

523

524 *Inversion Experimental Setup*

525 We use two approaches to compare numerical model outcomes against the stratigraphic
526 record. The first (experiment 1) is to compare the modeled and measured modern bathymetric
527 surface without taking into account the geometry of subsurface reflectors. This has the advantage
528 of simplicity as it does not require accounting for the post-deposition compaction of older
529 reflectors. The second approach (experiment 2) is to simultaneously compare between the model
530 and the data the position of all reflectors (except for the top of the basement/syn-rift deposits,
531 which is a boundary condition). This latter approach is more complicated, but provides a time-
532 integrated picture of model-data (mis)fit rather than relying on only the modern surface. The
533 multi-reflector approach may be particularly important when working with data from the SAM,
534 as the geometry of the uppermost layer (11-0 Ma) is thought to be heavily influenced by contour
535 currents in addition to processes transporting sediment seaward from the coast (Baby et al.,
536 2018). In both experiments, best-fit model parameter values are constrained for each section
537 independently. This approach allows comparison of best-fit parameter values among sections to
538 assess the variability of best-fit values across the SAM.

539 For each set of experiments, we also ran an inversion using a parameterization of our model
540 that collapses to the standard linear diffusion model by setting the sediment transport length scale
541 equal to the grid spacing and removing slope as a control on the sediment deposition rate.
542 Comparison of best-fit results between the nonlocal, nonlinear model and the local, linear model
543 will reveal whether the additional complexity we have implemented to approximate nonlocal,
544 nonlinear sediment transport leads to model results that better match observations from the SAM.

545 ***Experiment 1: Calculating misfit using the modern bathymetric surface.*** In this
546 experiment we compare the modeled bathymetric surface after 130 Ma to the bathymetric
547 surface revealed in Baby et al. (2019). Because the basement elevation at 130 Ma of model time

548 is imposed to match the observed basement elevation, this is equivalent to comparing the
549 observed (h_{obs}) and modeled (h_{sim}) thickness of sediment deposited at every point i along a
550 section. The misfit function can be written as:

551
$$\mu = \sqrt{\frac{1}{N-1} \sum_{i=1}^{N-1} \frac{(h_{obs}-h_{sim})^2}{\delta^2}}, \quad (13)$$

552 where N is the number of cells in the model domain—and the number of points to which the
553 seismic section has been downsampled—such that all points except for the boundary condition
554 tied to $z = 0$ are considered. δ is the error associated with our observations. Because we do not
555 have an explicit estimate of δ at every point, which would be a quantity derived during the
556 seismic interpretation process, the value of δ has no influence on the inversion process because
557 the divisor is constant throughout all of our experiments. Only in a case of spatially or
558 temporally varying δ would its value affect the search for a best-fit set of parameter values.

559 **Experiment 2: Calculating misfit using all reflectors.** Our second, more sophisticated
560 inversion scheme compares the elevation above basement of the eight reflectors from a given
561 seismic section against the same measurements from each modeled section. This comparison
562 gives rise to the misfit function:

563
$$\mu = \sqrt{\frac{1}{N_r(N-1)} \sum_{j=1}^{N_r} \sum_{i=1}^{N-1} \frac{(h_{obs}-h_{sim})^2}{\delta^2}}, \quad (14)$$

564 where N_r is the number of reflectors being compared between each measured and modeled
565 section (in our case $N_r = 8$).

566 The set of possible misfit functions for an inverse problem is infinite, necessitating
567 somewhat arbitrary choices. Our misfit functions are purely geometric—that is, they use deposit
568 shape alone. This is appropriate given the simplicity of our model, but we note that additional
569 constraints such as sand percentages derived from well-log data can allow the inference of

570 additional model parameters (e.g., Falivene et al., 2014). Other options for constructing misfit
571 functions include comparing deposit thickness or geometry at only a few key points (e.g., Yuan
572 et al., 2019a) or, if working in more than one planview dimension, comparing metrics of
573 planview margin geometry like the shelf edge (Zhang et al., 2021) or the stratigraphic centroid
574 (Martin et al., 2009; Granjeon, 2014).

575

576 **RESULTS AND DISCUSSION**

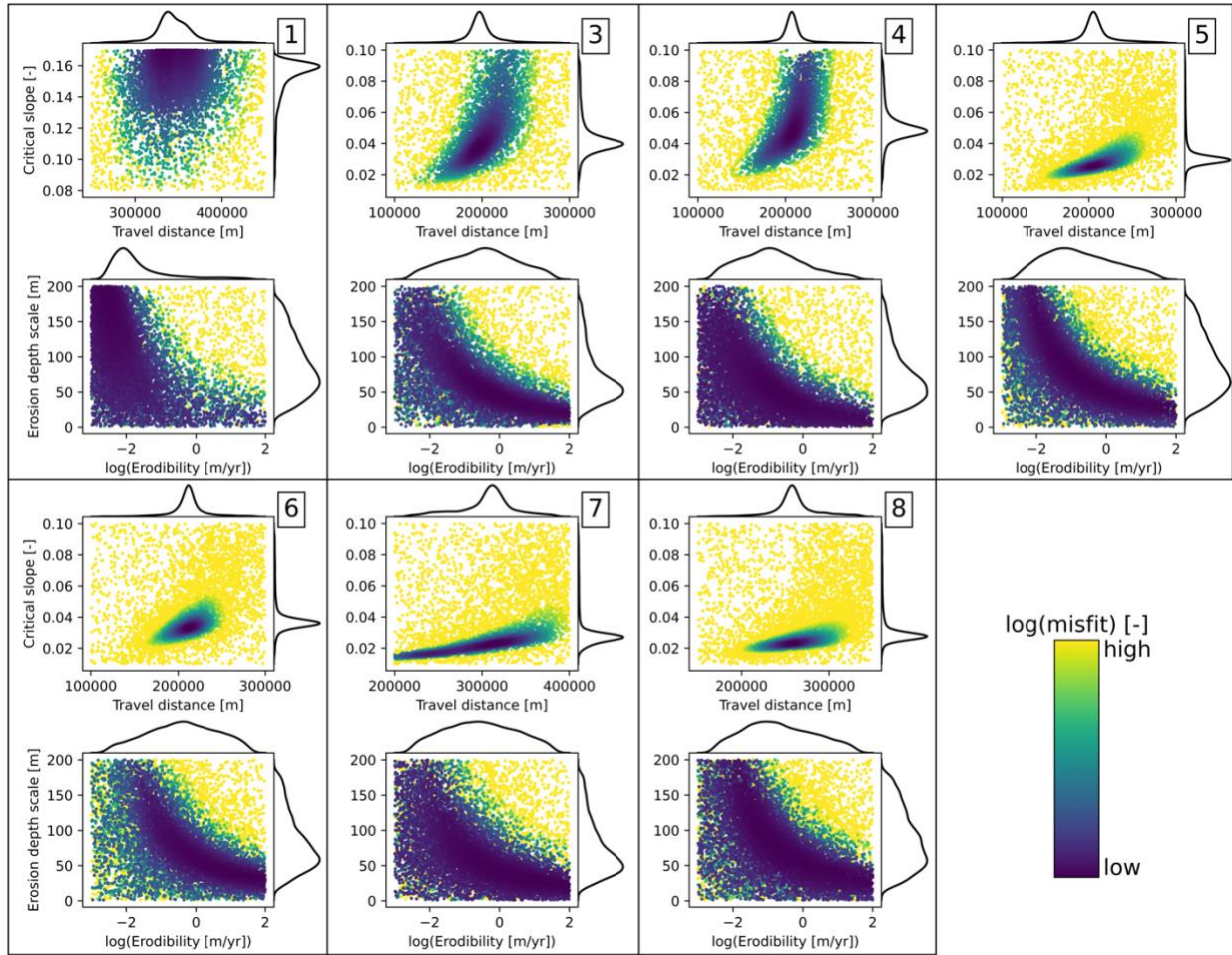
577 **The Nonlocal, Nonlinear Model Calibrated Against the Modern Bathymetric Surface**

578 *Best-fit Parameter Values*

579 Of the four parameters we varied in the nonlinear, nonlocal model, two dominate model
580 behavior and show narrow ranges that yield the best fit to the stratigraphic data (Figure 4, Table
581 S2). The two key parameters are the sediment transport distance and the slope of non-deposition.
582 Inversions converge on relatively narrow best-fit regions for these two values, such that
583 substantial deviation from the best-fit values results in much worse model-data fit. The same is
584 not true of the surface sediment erodibility and the erodibility depth scale. For all seven sections,
585 these parameters show large regions over which they provide fits of relatively unchanging
586 quality. This indicates that the sediment transport distance and slope of non-deposition drive
587 most of the variability in model outcomes. Physically, this suggests that it is the spatial pattern of
588 deposition, rather than remobilization of previously deposited sediments, that shapes the SAM.

589 Comparing parameter distributions across the seven sections (best seen in the kernel density
590 plots in Figure 4) reveals that every section converges on best-fit parameters that depart
591 significantly from the local, linear model. The majority of sections converge on values for the
592 sediment transport length scale of slightly over 2×10^5 m. Recalling that the local model is

593 recovered with a value of 10^4 m (our grid cell spacing), this result indicates that the shape of the
594 modern bathymetric surface in the SAM requires significant long-distance transport even across
595 low slopes. The best-fit slope of non-deposition is between ~ 0.02 and ~ 0.06 for all sections
596 except one—section 1—which has no portions of the parameter space that provide a good fit to
597 the data (Figure 5). Such low slopes of non-deposition imply a significant role for slope bypass,
598 or nonlocal downslope sediment transport. Best-fit S_c values many times the maximum slopes
599 observed on the SAM would indicate that sediment transport can be reasonably approximated by
600 transport that depends only on local slope (because sediment bypass becomes negligible when
601 $S \ll S_c$; equation 8, Figure 1). Given that our inverse analyses reveal S_c values ranging from
602 ~ 0.02 to ~ 0.06 in the sections where we find reasonable model-data fit, we do not find support
603 for the local transport approximation. Instead, the best fit between modeled and measured
604 stratigraphy is achieved when sediment can bypass slopes of more than a few degrees.



605

606 **Figure 4: Results for all seven sections from the search for a best-fit parameterization of the nonlocal,**
 607 **nonlinear model with the inversion procedure constrained only by the modern bathymetric surface. Scatter**
 608 **plots show model-data misfit (color) as a function of the four key parameters. Kernel density estimate (KDE)**
 609 **plots show the distribution of values for each parameter. Because the inversion procedure runs more model**
 610 **realizations in regions of the parameter space with reduced model-data misfit, peaks in the KDE plots can be**
 611 **interpreted as showing the region of each parameter's range that leads to the lowest misfit. Narrow peaks in**
 612 **the KDE plots indicate parameters with well-constrained best-fit values, while broad peaks indicate**
 613 **parameters for which a wide range of values produces similar misfit. Numbered sets of plots refer to the**
 614 **seismic section used for the inversion. Maximum and minimum misfit values vary between sections; color**
 615 **values have been scaled for interpretability.**

616

617 *Comparison of Modeled and Observed Stratigraphy*

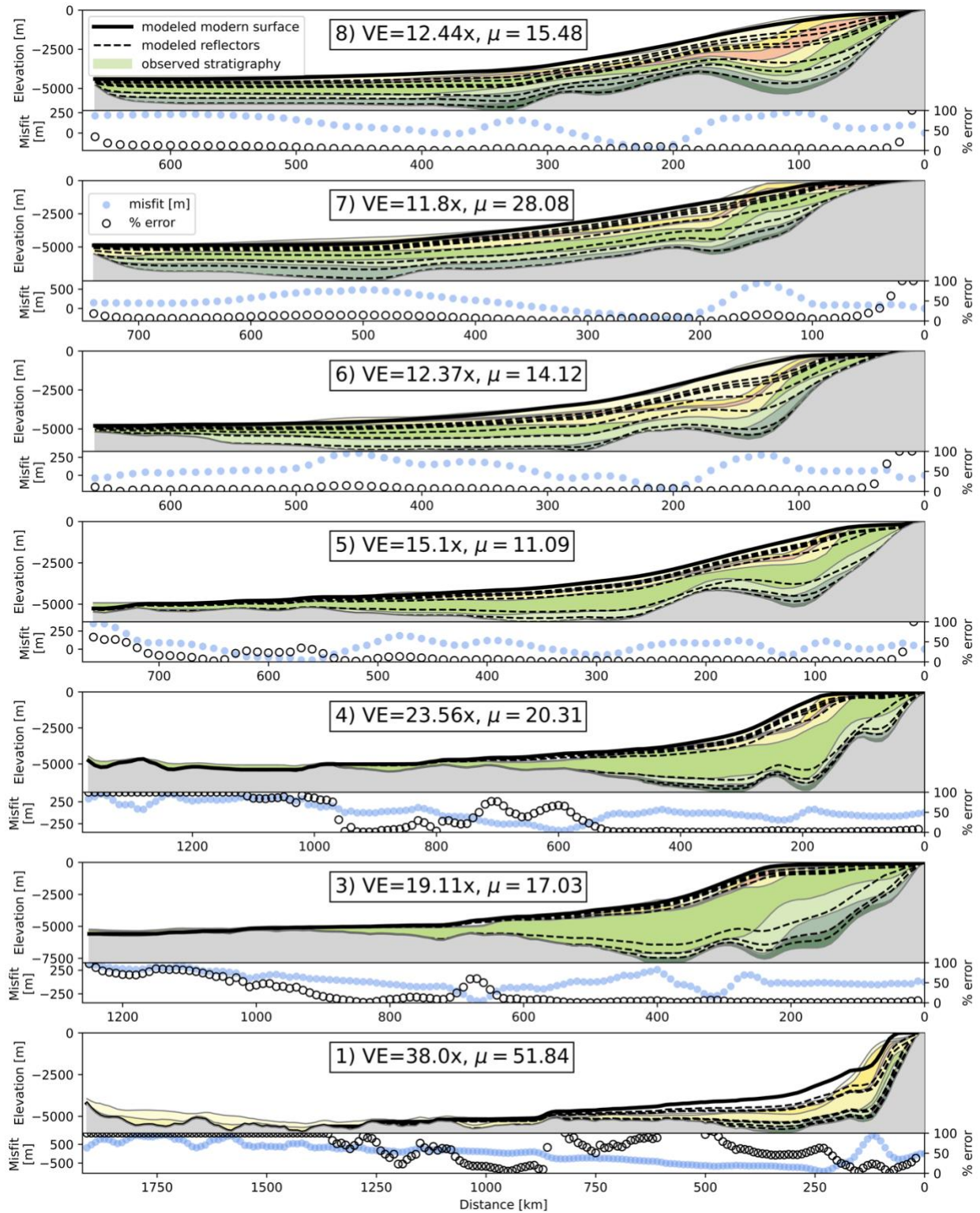
618 For five of the seven sections, the inversion yielded best-fit parameter estimates that led to
 619 best-fit simulations that qualitatively and quantitatively fit the data reasonably well (Figure 5).

620 These sections have gently sloping continental shelves with altitudes below, rather than level
 621 with, sea level, and smooth, convex-up shelf edges. They have concave-up continental slopes

622 grading into gently sloping continental rise/abyssal plain deposits. Sediment is not always found
623 as far from shore as in the data, but noticeable accumulations of sediment are observed up to
624 ~1000 km from shore. Two sections, 1 and 7, yielded what we interpret to be substantially worse
625 fits as defined by the mismatch of major morphometric features like the continental shelf edge
626 and the curvature of the continental slope. It is difficult to know why the fits are substantially
627 worse for sections 1 and 7. One key commonality that the two sections share is a relatively high
628 proportion of the total sediment volume stored at the extreme distal end of the section. While our
629 approach does allow for more realistic modeling of long-runout sediment transport than the
630 classic local, linear approach does, there is still a fundamental tension in which allowing
631 sediment to accumulate at the very distal end of the modeled section requires too much inhibition
632 of deposition at the proximal end. It may not be possible for our model to deposit enough
633 sediment in distal reaches while preserving steep, well-defined shelf edges. This weakness would
634 not be resolved in section 1 by raising the maximum possible S_c value (Figure 4); increases in S_c
635 would further inhibit transport to the basin floor.

636 Comparison of modeled and observed subsurface reflectors, though it was not quantitatively
637 incorporated into the misfit function in this experiment, shows that the pattern of reflectors is
638 almost completely depositional. There are few—and only minor—instances of reflectors being
639 truncated by overlying units, indicating that the story in these models is one of continuous
640 deposition rather than episodes of deposition and re-erosion driven by variations in the terrestrial
641 sediment flux time series. This is broadly concordant with the interpreted geologic history of the
642 SAM, in which—barring the episodes of rock uplift that we have not modeled here—there is
643 little erosional truncation of units except by eustatic variations in the nearshore. This
644 concordance of modeled and observed stratigraphy suggests that our model is not only producing

645 reasonable final bathymetry, but is building a stratigraphic record that reflects the long-term
646 average of the processes shaping the SAM.



647
 648 **Figure 5: Comparison between modeled and measured stratigraphy for all seven sections with two measures**
 649 **of misfit. While all modeled reflectors are shown (and are compacted to account for overburden), only the**
 650 **modern bathymetric surface was used to assess model-data fit in this experiment; subsurface modeled**
 651 **reflectors were not compared against data to assess fit. Percent error points that appear to be missing are**

652 >100%; Values of exactly 100% error typically occur where the model deposited no sediment. μ is total misfit
653 given by equation 13; VE is vertical exaggeration.
654

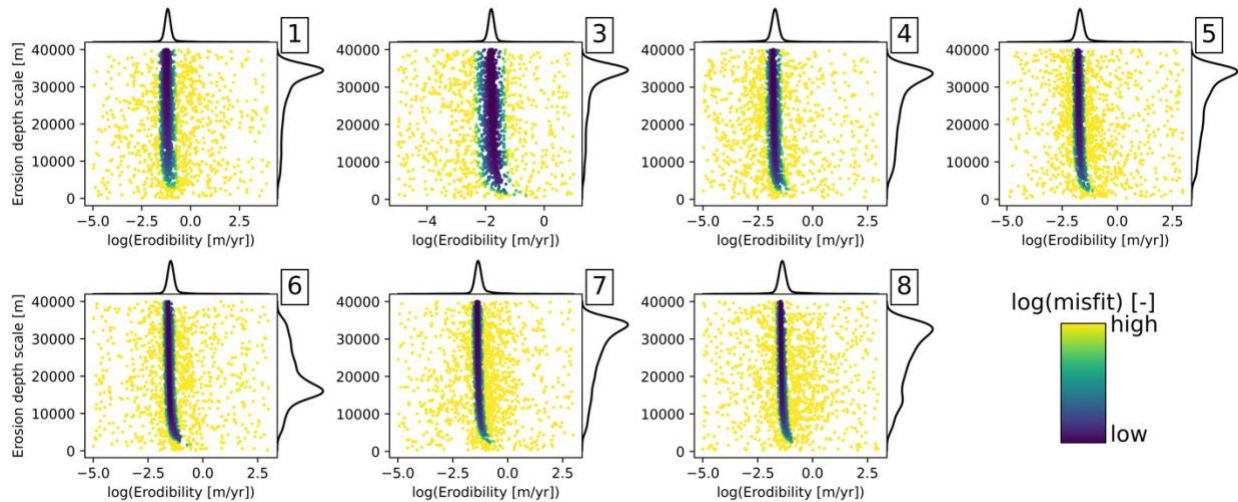
655 **Comparison Between the Nonlocal, Nonlinear Model and the Local, Linear Model**

656 Here we compare inversion results between the two models to assess whether the nonlocal,
657 nonlinear model leads to substantially better fits between modeled and measured stratigraphy.
658 We search for the best-fit local, linear model using the same procedure as for our new model; the
659 only two parameters to optimize in the local, linear model are the surface sediment erodibility K_e
660 and the depth scale over which it decays d_* .

661 Using only the modern bathymetric surface as a constraint, the local, linear model converges
662 to a narrow range of surface erodibility values and a broader region of erodibility decay depths
663 for sections 3-8 (Figure 6, Table S2). Section 1, ever the outlier, converges on a large erodibility
664 value that decays rapidly with depth. All sections except section 6 indicate that the model is
665 “searching” for erodibility decay depth values even greater than the 40,000 m maximum value in
666 the inversion. At the maximum values of 40,000 m, erodibility in the deepest parts of the margin
667 only declines to ~80% of its value at the water surface such that sediment entrainment can still
668 occur in the deep, distal reaches of the margin wherever nonzero slopes are found. We interpret
669 this behavior as the local, linear model compensating for its lack of mechanisms for long-
670 distance sediment transport by allowing substantial erosion at great depth. Interestingly, the
671 tendency of the inversion procedure to identify d_* values large enough that sediment erodibility
672 does not meaningfully decline with depth suggests that while erodibility decay with depth may
673 give rise to realistic-looking shallow marine morphometric features like shelf breaks (Kaufman
674 et al., 1992; van Balen et al., 1995), such an approach may ultimately be counterproductive when
675 we expand our view to include the distal portion of the margin because it yields models that

676 cannot transport sediment far enough from shore without some other process or additional
677 changes in erodibility with depth or distance from shore.

678



679

680 **Figure 6: Results for all seven sections from the search for best-fit parameter values for the local, linear**
681 **diffusion model constrained only by the modern bathymetric surface. The tall, narrow region of good-fitting**
682 **models indicates that only a narrow range of surface erodibility values leads to minimized misfit. The**
683 **majority of sections (all except 6) have converged to the maximum values of the erodibility decay depth scale,**
684 **indicating that even higher values would lead to further improvements in model-data fit. Given that under**
685 **our imposed maximum value of 40,000 m, erodibility in the deepest regions of the margin only declines to**
686 **~80% of its value at the water surface, further improvements to model-data fit from increasing the maximum**
687 **decay depth would be marginal.**
688

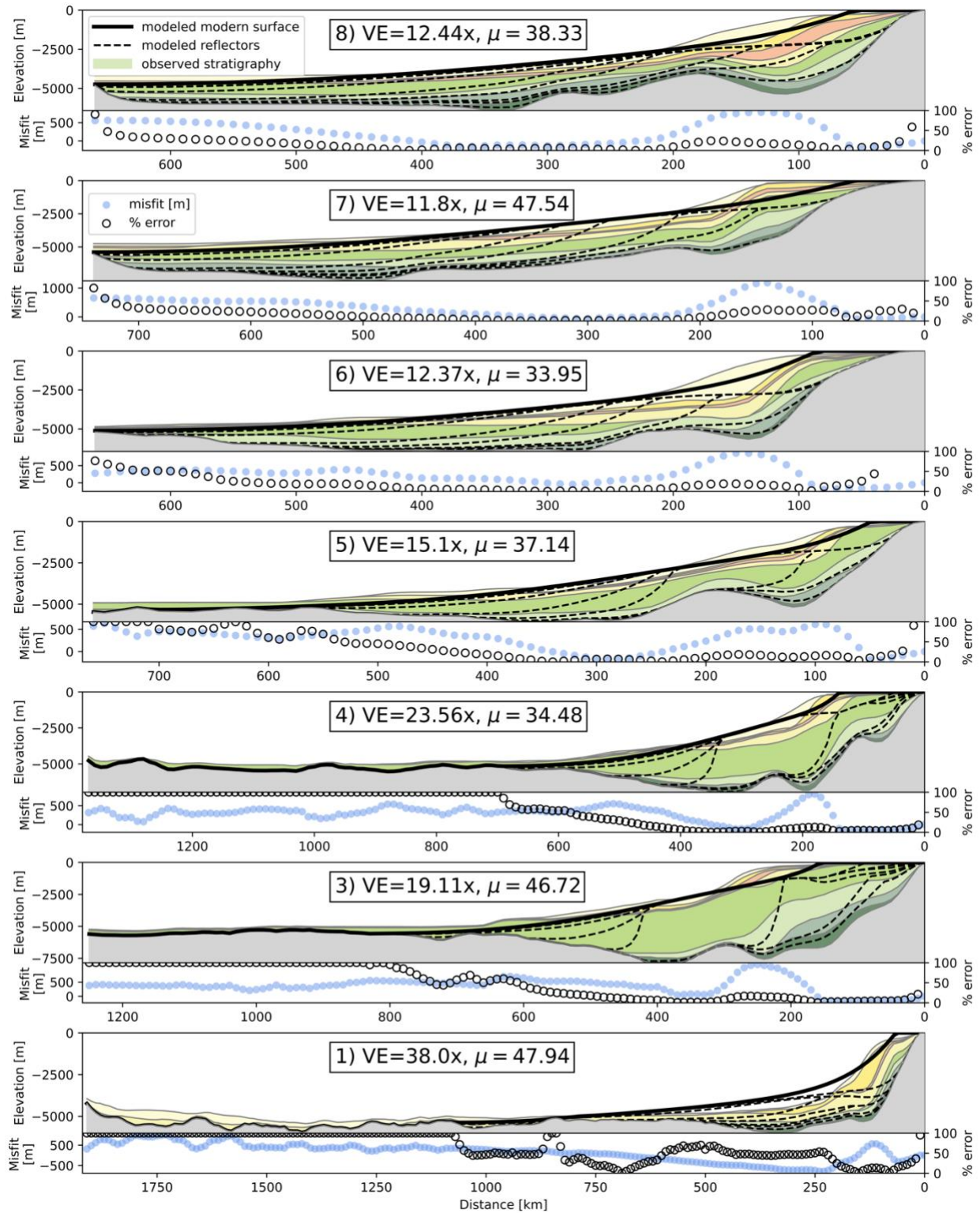
689 The local, linear model provides, for all sections that can be reasonably fit by either
690 approach, a worse fit to the modern bathymetric surface than was obtained with the nonlocal,
691 nonlinear model (Figure 7, 8). While best-fit parameterizations of the local, linear model do
692 exhibit sediment delivery to the distal portions of the sections (achieved through large erodibility
693 decay depths that yield non-negligible erodibility at depth), this comes at the cost of model-data
694 fit in the nearshore environment. The large erodibility decay depths required to enable transport
695 of sediment far from shore precludes the local, linear model from achieving the rounded, shallow
696 continental shelf edge observed in the data. Instead, a shelf of sorts is created simply by
697 progradation of the shoreline as sediments accumulate in the nearshore but are prevented from

698 accumulating above sea level under the assumption that the shoreline will prograde under such
699 conditions. Shoreline progradation, combined with an erodibility that is nearly constant
700 throughout the depth profile, results in sharp shelf breaks grading immediately into the concave-
701 up continental slope rather than the smooth, convex-up shelf breaks observed in the seismic data.
702 The local, linear model is effectively being forced to choose between accurately reproducing the
703 shelf edge and delivering sediment to the distal portions of the margin. Because our misfit
704 function incorporates every point along each section, the model minimizes misfit if it delivers
705 sediment far from shore even at the cost of reproducing the shelf and shelf-edge. A misfit
706 function that focused on the nearshore (e.g., Yuan et al., 2019a) would likely lead to the opposite
707 end-member of this tradeoff.

708 Though our misfit function in this experiment did not incorporate comparison between
709 observed and modeled subsurface reflectors, the local, linear model—even in its best-fit
710 parameterizations—does not stand up to a qualitative assessment of the form of the subsurface
711 reflectors it produces (Figure 7). To deliver sediment far from shore, the local, linear model must
712 first deposit that sediment in a proximal location and then erode those deposits during times of
713 low terrestrial sediment flux. The time series of reflectors produced in most of the local, linear
714 best-fit simulations reveal a steep, prograding wedge of sediment that is then smoothed out to
715 lower gradients through subsequent erosion. Except for the brief periods in SAM history when
716 the margin experienced substantial rock uplift, which we do not model, there is limited evidence
717 for significant erosional truncation beyond that occurring in the nearshore due to eustatic
718 variations (Baby et al., 2018). The reflectors from the nonlocal, nonlinear model (Figure 5) do
719 not show this pattern of progradation of a steep-fronted sediment wedge followed by later
720 truncation by erosion; they instead show consistent accumulation of sediments through time at

721 any given location, including the distal reaches of the basin. Interpretation of the stratigraphic
722 record suggests that the latter behavior is more consistent with the history of the SAM.

723 It is unsurprising that the nonlocal, nonlinear model provides a better fit to the data than the
724 local, linear model (Figure 8) in all but one case where neither model provided a reasonable fit
725 and imposed parameter ranges prevented the more complex model from fully minimizing misfit
726 (Figure 4)—the latter model is a restricted subset of the former. The critical results of this
727 comparison are that (1) the model requires significant deviation from linear diffusion parameter
728 values (i.e., a large travel distance relative to the model grid cell spacing and a critical slope low
729 enough that sediment bypass is common) to provide a reasonable match between modeled and
730 observed bathymetry, (2) the local, linear model cannot through parameter adjustments provide
731 fits that approximate the outcomes of the nonlocal, nonlinear model, (3) the dynamics of the
732 local, linear model as revealed by subsurface reflectors are not supported by observations from
733 the SAM, and (4) seven of eight sections show a reduction in misfit—and four of seven sections
734 show at least a factor of two reduction—achieved by adding nonlocal, nonlinear transport
735 dynamics (Figure 8). This suggests that long-distance transport and slope-dependent sediment
736 bypass processes are required to form the canonical shapes of passive margin stratigraphy, and
737 therefore argues that these processes are essential ingredients in SFMs, at least for passive
738 margin settings.



739

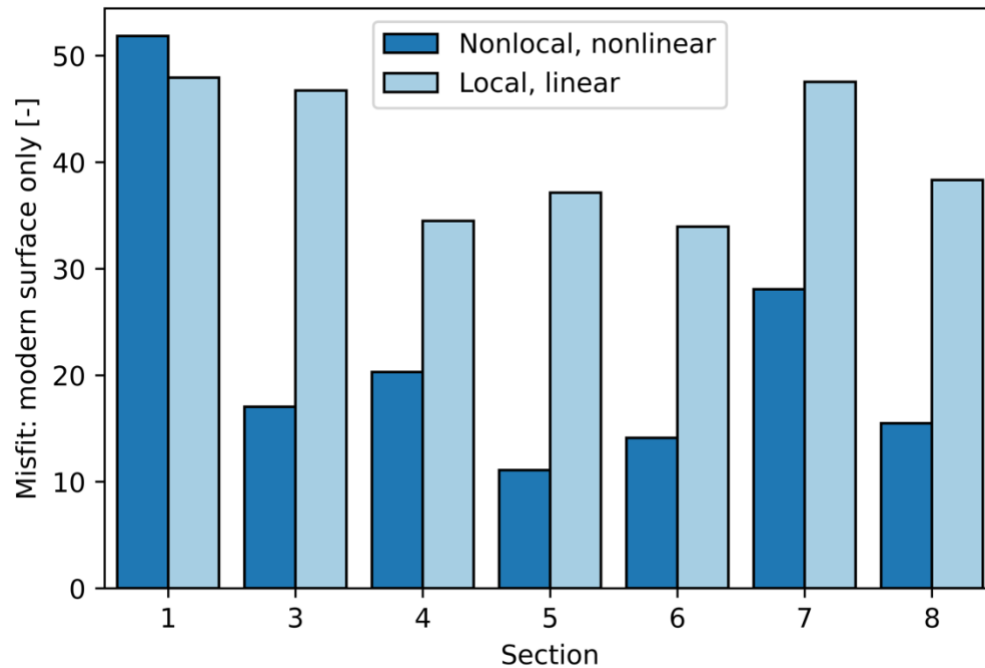
740

741

742

Figure 7: Comparison between modeled and measured stratigraphy for the best-fit local, linear diffusion model realization for each section. Bottom panels show two measures of misfit. While all modeled reflectors are shown (and are compacted to account for overburden), only the modern bathymetric surface was used to

743 assess model-data fit in this experiment; subsurface modeled reflectors were not compared against data to
744 assess fit. μ is total misfit given by equation 13; VE is vertical exaggeration.
745



746 **Figure 8: Misfit values for the best-fit model for each section using the nonlocal, nonlinear model (dark blue)**
747 **and the local, linear model (light blue) when the model fit is determined by comparing only against the**
748 **modern bathymetric surface. The nonlocal, nonlinear model yields better fitting best-fit realizations for six of**
749 **seven sections.**
750
751

752 **The Influence of Considering Multiple Reflectors**

753 Parameters estimated by the inversion that takes into account all eight reflectors are surprisingly
754 similar to those estimated when using only the modern bathymetric surface to constrain the
755 inversion. For brevity we show average parameter values for the 50 best-fitting model
756 realizations from the single reflector and multiple-reflector inversions plotted against each other
757 (Figure 9) such that points falling on the 1:1 line indicate consistent parameter values achieved
758 by the two methods. See Table S3 and Figures S1-S4 for detailed results of multi-reflector
759 inversions.

760 Inclusion of all reflectors in the misfit calculation for the nonlocal, nonlinear model
761 resulted in a shift towards slightly greater best-fit travel distance values (Figure 9A), likely

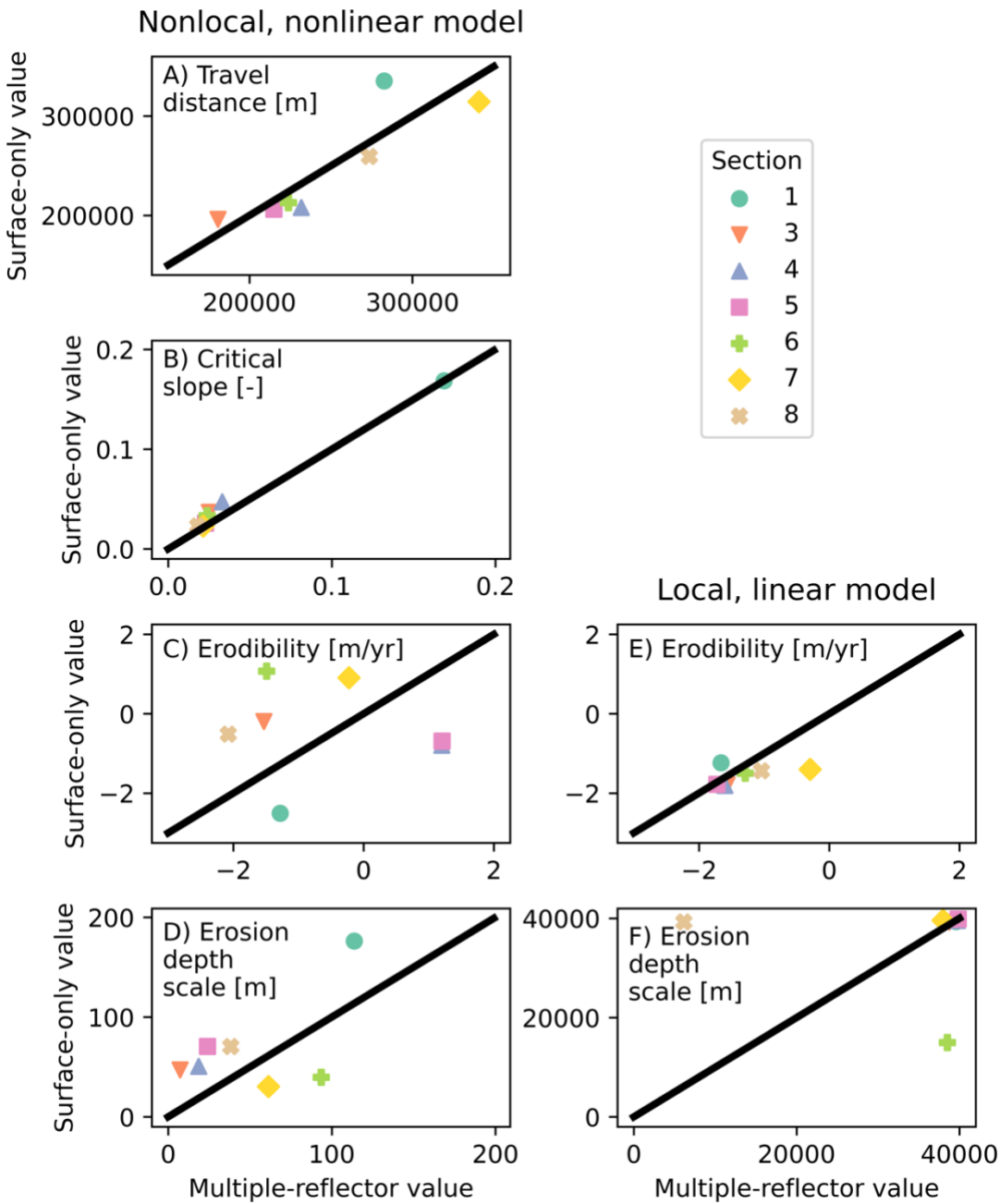
762 because the data requires that good-fitting models be able to distribute sediment to the distal
763 portion of the basin even relatively early in the margin's evolution when there do not yet exist
764 the slopes required to drive sediment bypass in the absence of another mechanism for long-
765 distance transport. The critical slope of non-deposition (Figure 9B) remained remarkably
766 consistent between the surface-only and multiple-reflector inversions, suggesting that the model
767 most effectively adjusts to the need to deliver early deposits far from shore with changes in the
768 travel distance, which affects transport over all slopes, rather than the critical slope, which only
769 affects transport over meaningful gradients. Physically this may indicate the importance of long-
770 runout sediment transport processes (e.g., turbidity currents, marine debris flows) that may
771 initially be generated by significant bathymetric slopes but then transport sediment up to
772 hundreds of km over vanishingly low slopes. The erodibility and erosion depth scale (Figure 9C
773 and D, respectively) show more scatter between inversion methods; this is not surprising given
774 that there is a large region of good-fitting values for both parameters (e.g., Figure 4).

775 Including all reflectors when searching for best-fit parameters for the local, linear model
776 leads to surface erodibility values that largely fall near the 1:1 line (Figure 9E), indicating that
777 the composition of the misfit function did not have a strong effect on the best-fit value. The same
778 is true of the erodibility decay depth scale (Figure 9F) with the exception of two values that
779 changed significantly between the surface-only and multiple-reflector inversion schemes. We
780 attribute the overall consistency between parameter values derived using the two different
781 methods to the fact that all reflectors in our seismic data show a similar pattern: long-distance
782 transport beginning from the earliest stages of post-rift margin evolution followed by the largely
783 depositional draping of successive units atop previous deposits. In this respect the modern
784 surface is not geometrically distinct from the subsurface reflectors, which may explain why

785 incorporating the subsurface reflectors leads to little improvement in model-data fit. A model can
786 either achieve parameter values that allow it to develop these types of deposits (i.e., in the
787 nonlocal, nonlinear model) in which case the specific number and age of reflectors used does not
788 have a significant effect on inferred best-fit parameter values, or it cannot achieve
789 parameterizations that allow long-distance, deposition-driven stratal stacking patterns (i.e., in the
790 local, linear model) in which case the specifics of the misfit function do not matter because the
791 fit to eight reflectors will be no better than the fit to a single one. We initially undertook the
792 multiple-reflector inversion because the modern bathymetric surface is thought to be heavily
793 influenced by contour currents (Baby et al., 2018). Adding seven subsurface reflectors does not
794 substantially change inferred best-fit parameters, which may indicate that variability in contour
795 current effects among units does not cause a radical enough change in stratigraphic
796 architecture—relative to the effects of subsidence and terrestrial sediment flux—to influence our
797 simple models.

798 When the misfit function incorporates all eight reflectors, the nonlocal, nonlinear model
799 yields a better fit to the observed stratigraphic data than the local, linear model does for all seven
800 sections (Figure 10). The improvement in model-data fit gained from adding nonlocal, nonlinear
801 sediment transport dynamics exists regardless of whether we use only the modern surface or all
802 reflectors as a basis for comparison. The misfit values between the two models are much closer
803 when all reflectors are used for the inversion (Figure 10). This arises from the introduction of
804 seven additional constraints on the model, many of which it must inevitably fail to match (Figure
805 5) even in its best-fit parameterization. However, the consistent reduction in misfit that
806 accompanies the nonlocal, nonlinear model signals that those dynamics are required to produce
807 stratigraphy that matches observations. The only scenario where this would not hold true is one

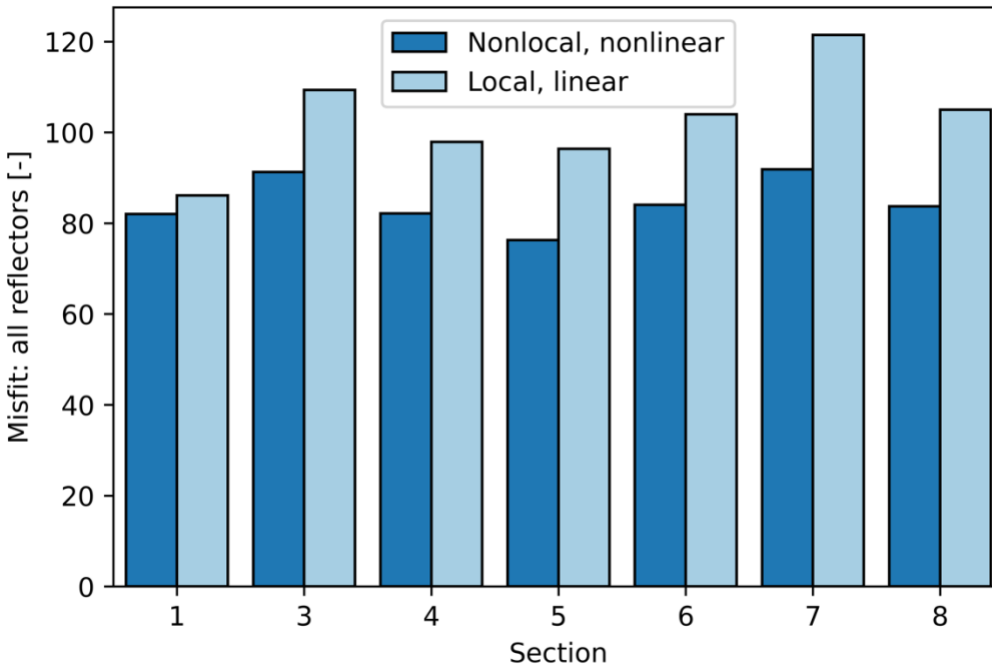
808 in which a misfit function was used that did not take into account the distal portions of the basin
 809 at all. Given the substantial accumulations of sediment in the distal portions of the SAM (Figure
 810 2), we argue that finding models that adequately simulate those deposits is a prerequisite for
 811 closing the source-to-sink mass balance.



812

813 **Figure 9: Comparison between best-fit parameter values derived from the surface-only inversion and the**
 814 **multiple-reflector inversion. Black lines indicate a 1:1 match between parameter values derived by the two**

815 methods. In the case of the nonlinear, nonlocal model (column 1), the two most important parameters fall
816 close to the 1:1 line, indicating that the inversion method (whether subsurface information is incorporated or
817 not) does not have a strong influence on the best-fit parameter values and therefore on predicted margin
818 stratigraphy. In the case of the local, linear model (column 2), erodibility values are consistent between
819 methods while erosion depth scale values show more scatter.
820



821
822 **Figure 10: Misfit values for the best-fit model for each section using the nonlocal, nonlinear model (dark blue)**
823 **and the local, linear model (light blue) when the model fit is determined by comparing against all seismic**
824 **reflectors. The nonlocal, nonlinear model yields better fitting best-fit realizations for all seven sections.**
825

826 Limitations and Implications for Inversion of the Stratigraphic Record

827 Our motivation in testing SFMs is to enable the inversion of the stratigraphic record for
828 information about past terrestrial environments and geomorphic processes. If reasonably
829 effective SFM structures and parameterizations can be identified *a priori*, then coupled
830 LEM/SFMs will be more useful for inferring drivers of past landscape evolution. Our results
831 favor the idea that SFMs should incorporate mechanisms for sediment bypass and long-distance
832 transport, and that these processes cannot be adequately mimicked with parameter changes in the
833 commonly used local, linear diffusion model for seascape evolution. Our study further
834 emphasizes that *both* mechanisms of nonlocality (bypass and long-distance transport) are

835 required to achieve the model-data agreement we find; Figure 4 demonstrates that one element or
836 the other is not sufficient to place the model in the good-fitting region of the parameter space.

837 The nonlocal, nonlinear model we tested represents an amalgamation of ideas from
838 previous workers that have not previously been evaluated in detail against stratigraphic data, and
839 our analysis reveals that it provides a substantial improvement over the more widely used local,
840 linear model. However, the nonlocal, nonlinear model still needs improvement. Aside from
841 subsuming a wide array of marine transport processes into two key transport parameters, its most
842 critical shortcoming is that it only heuristically accounts for the momentum that allows transport
843 processes like turbidity currents and marine debris flows to carry sediment into the distal
844 portions of basins. More effective conceptualizations of sediment entrainment and
845 disentrainment, possibly following recent advances in hillslope geomorphology (e.g., Doane et
846 al., 2018; Furbish et al., 2021), might further improve SFMs with the understanding that the
847 models will always need to simulate the spatial and temporal average of marine sediment
848 transport if they are to prove feasible for inverse analyses that require 10^5 - 10^6 forward model
849 realizations. Improving model fit—especially abrupt slope breaks driven by changes in process
850 dominance—may require multiprocess models (e.g., Granjeon et al., 1999; Syvitski and Hutton,
851 2001), but their parameter-rich nature may hinder parameter estimation exercises and make them
852 susceptible to overfitting to a given calibration location. There exist sufficient models in the
853 literature that span a wide range of complexity that, as in this study, the future challenge is more
854 about rigorously testing models against data to find the simplest workable theory than it is about
855 developing new models.

856 Though we used seven seismic sections spanning four basins to evaluate different SFMs,
857 our study is limited to a single passive margin. Best-fit regions of the parameter space for the

858 nonlinear, nonlocal model's travel distance and critical slope of non-deposition parameters
859 consistently showed that the model was not collapsing to its local, linear parameterization, but
860 the key parameters still exhibited considerable variability among sections (Figure 4). While our
861 analysis may have restricted the range of possible values that need to be considered when using
862 such a model to invert the stratigraphic record, a set of global parameter values cannot be
863 assumed. Similarly, we have not established sensitivity of inversion outcomes to initial and
864 boundary conditions and additional processes—including eustatic sea level, lithospheric flexure,
865 and terrestrial sediment supply—which are well-understood in the SAM relative to other regions
866 but still carry considerable uncertainty (e.g., Guillocheau et al., 2012).

867 Flexure is a process of particular interest given that it can influence the location of
868 depocenters and resulting stratal geometries. We have not treated flexure here to ensure that
869 modeled stratigraphy is compared in the context of a consistent time-evolving basement
870 geometry. We suspect that adding flexure to the model would not alter the conclusion that
871 nonlocal processes govern the development of passive margin stratigraphy. The generally
872 proximal deposition in the local, linear model (Figure 7) might cause flexural subsidence in those
873 locations, thereby potentially reducing bathymetric slopes and resulting fluxes of sediment
874 towards the distal portions of the basin. The longer-distance deposition given by the nonlocal,
875 nonlinear model (Figure 5) may result in less proximal flexural subsidence and the maintenance
876 of greater bathymetric slopes, allowing enhanced transport towards the deep, distal portions of
877 the margin. Nonetheless, the relative importance of nonlocal transport processes in models
878 including flexural subsidence is important to examine.

879 A final open question is the applicability of our findings given the reduced
880 dimensionality of our modeling exercise. We tested 2-D implementations of our candidate

881 models. This means that the models enforced purely margin-perpendicular sediment transport,
882 when in reality margin-parallel components of transport—such as contour currents that are
883 known to have influenced the SAM (Baby et al., 2018)—also occur. Our 2-D implementations
884 also cannot simulate processes that cause the development of preferential sediment transport
885 pathways, like submarine canyons and channels. We therefore must interpret the improvement in
886 fit given by our nonlocal, nonlinear model as arising due to the model’s ability to simulate
887 average sediment transport patterns that occur as a result of nonlocal processes whose effects
888 likely vary spatially over geologic time, like for example a submarine channel undergoing
889 avulsions across a deep-sea fan. Though there exist plenty of 3-D SFMs (e.g., Granjeon and
890 Joseph, 1999; Salles et al., 2018; Falivene et al., 2019), testing optimal SFM structure in two
891 dimensions remains an important stepping stone towards inverting terrestrial landscape history
892 from stratigraphy because the simplicity and parsimony of 2-D models allows relatively efficient
893 calibration even in data-poor situations.

894

895 **CONCLUSIONS**

896 We evaluated a simple, nonlocal, nonlinear model for marine sediment transport and the
897 development of marine stratigraphy over geologic time. The model builds on the concepts of
898 sediment bypass espoused by previous authors (e.g., Syvitski et al., 1998; Ross et al., 1994; Ding
899 et al., 2019a;) that have not previously been directly tested against observed stratigraphy.

900 Quantitative comparison of the model against seven stratigraphic sections from the SAM reveals
901 that:

- 902 1. The nonlocal, nonlinear model can achieve parameterizations that develop realistic
903 marine bathymetry and stratigraphy, though variability in best-fit parameter values exists
904 among the seven seismic sections tested.
- 905 2. The nonlocal, nonlinear model does not converge on parameter values that result in a
906 collapse to the local, linear model. The local, linear model cannot fit the data. It fails both
907 to fit the modern bathymetric surface and to yield seascape evolution trajectories that
908 match observations.
- 909 3. The key difference between the two models lies in the ability of the nonlocal, nonlinear
910 model to deliver sediment to distal portions of the basin without compromising its ability
911 to develop realistic nearshore morphology and stratigraphy.
- 912 4. Points (1) through (3) hold true regardless of whether model parameters are optimized
913 using only the modern bathymetric surface or the full suite of subsurface seismic
914 reflectors, indicating that our results are robust to the specifics of the misfit function
915 employed.
- 916 5. Processes of sediment bypass and long-distance transport govern the architecture of the
917 stratigraphic record over basin-filling timescales, making it essential that SFMs capture at
918 least the spatial and temporal averages of these nonlocal processes.

919

920 Given the general lack of terrestrial evidence for past landscape evolution dynamics, the
921 stratigraphic record represents our best chance to learn about the erosion trajectories of
922 landscapes long gone. We tentatively suggest that the transport dynamics encapsulated in the
923 nonlocal, nonlinear model govern the development of passive margin stratigraphy. Our ability to
924 invert the stratigraphic record, either on its own for inferring sediment supply to basins or

925 coupled with landscape evolution models to infer past tectonic, climatic, and/or lithologic
926 boundary conditions, would benefit from improved understanding of such nonlocal transport
927 processes.

928

929 **DATA AVAILABILITY STATEMENT**

930 The data and code that support the findings of this study are openly available on Figshare at
931 <https://doi.org/10.6084/m9.figshare.20205077>.

932

933 **ACKNOWLEDGMENTS**

934 C.M. Shobe was supported by H2020 Marie Skłodowska-Curie Actions grant no. 833132
935 (STRATASCAPE). We acknowledge time on the West Virginia University Thorny Flat high-
936 performance computing cluster which is supported by the National Science Foundation under
937 Major Research Instrumentation program award #1726534. We thank Benoît Bovy, Tim Carr,
938 Rachel Glade, Kim Huppert, Luca Malatesta, Delphine Rouby, Jaime Toro, and Amy Weislogel
939 for helpful discussions. Thanks to Guillermo Franco, Nate Garver-Daniels, and Daniel Turpen
940 for HPC support and to Xuesong Ding, Oriol Falivene, and Associate Editor Peter Burgess for
941 constructive reviews.

942

943 **REFERENCES CITED**

944 Aizawa, M., Bluck, B., Cartwright, J., Milner, S., Swart, R., and Ward, J., 2000, Constraints on
945 the geomorphological evolution of Namibia from the offshore stratigraphic record,
946 Communications of the Geological Survey of Namibia, v. 12, p. 337—346.

- 947 Allen, P.A. and Allen, J.R., 2013, Basin Analysis, Principles and Application to Petroleum Play
948 Assessment, Wiley-Blackwell, 632 p.
- 949 Andrews, D.J. and Bucknam, R.C., 1987, Fitting degradation of shoreline scarps by a nonlinear
950 diffusion model, *Journal of Geophysical Research: Solid Earth*, v. 92, no. B12, p. 12857—
951 12867, doi:10.1029/JB092iB12p12857.
- 952 Baby, G., Guillocheau, F., Morin, J., Ressouche, J., Robin, C., Broucke, O., and Dall'Asta, M.,
953 2018, Post-rift stratigraphic evolution of the Atlantic margin of Namibia and South Africa:
954 Implications for the vertical movements of the margin and the uplift history of the South
955 African Plateau, *Marine and Petroleum Geology*, v. 97, p. 169—191,
956 doi:10.1016/j.marpetgeo.2018.06.030.
- 957 Baby, G., Guillocheau, F., Braun, J., Robin, C., and Dall'Asta, M., 2019, Solid sedimentation
958 rates history of the Southern African continental margins: Implications for the uplift
959 history of the South African Plateau, *Terra Nova*, v. 32, no. 1, p. 53—65,
960 doi:10.1111/ter.12435.
- 961 van Balen, R.T., van der Beek, P.A., and Cloetingh, S.A.P.L., 1995, The effect of rift shoulder
962 erosion on stratal patterns at passive margins: Implications for sequence stratigraphy, *Earth
963 and Planetary Science Letters*, v. 134, p. 527—544, doi:10.1016/0012-821X(95)98955-L.
- 964 Barnhart, K.R., Glade, R.C., Shobe, C.M., and Tucker, G.E., 2019, Terrainbento 1.0: a Python
965 package for multi-model analysis in long-term drainage basin evolution, *Geoscientific
966 Model Development*, v. 12, p. 1267—1297, doi:10.5194/gmd-12-1267-2019.
- 967 Barnhart, K.R., Tucker, G.E., Doty, S., Shobe, C.M., Glade, R.C., Rossi, M.W., and Hill, M.C.,
968 2020a, Inverting topography for landscape evolution model process representation: Part 1,

- 969 conceptualization and sensitivity analysis, *Journal of Geophysical Research: Earth Surface*,
970 v. 125, no. 7, doi:10.1029/2018JF004961.
- 971 Barnhart, K.R., Tucker, G.E., Doty, S., Shobe, C.M., Glade, R.C., Rossi, M.W., and Hill, M.C.,
972 2020b, Inverting topography for landscape evolution model process representation: Part 2,
973 calibration and validation, *Journal of Geophysical Research: Earth Surface*, v. 125, no. 7,
974 doi:10.1029/2018JF004963.
- 975 Barnhart, K.R., Tucker, G.E., Doty, S., Shobe, C.M., Glade, R.C., Rossi, M.W., and Hill, M.C.,
976 2020c, Inverting topography for landscape evolution model process representation: Part 3,
977 determining parameter ranges for select mature geomorphic transport laws and connecting
978 changes in fluvial erodibility to changes in climate, *Journal of Geophysical Research: Earth*
979 *Surface*, v. 125, no. 7, doi:10.1029/2019JF005287.
- 980 Beaumont, C., Fullsack, P., and Hamilton, J., 1992, Erosional control of active compressional
981 orogens, *in* McClay, K.R., ed., *Thrust tectonics*, p. 1—18.
- 982 van der Beek, P., and Bishop, P., 2003, Cenozoic river profile development in the Upper Lachlan
983 catchment (SE Australia) as a test of quantitative fluvial incision models, *Journal of*
984 *Geophysical Research: Solid Earth*, v. 108, no. B6, doi:10.1029/2002JB002125.
- 985 Bessin, P., Guillocheau, F., Robin, C., Braun, J., Bauer, H., and Schroëtter, J.-M., 2017,
986 Quantification of vertical movement of low elevation topography combining a new
987 compilation of global sea-level curves and scattered marine deposits (Armorican Massif,
988 western France), *Earth and Planetary Science Letters*, v. 470, p. 25—36,
989 doi:10.1016/j.epsl.2017.04.018.
- 990 Bornholdt, S., and Westphal, H., 1998, Automation of stratigraphic simulations: quasi-backward
991 modeling using genetic algorithms, *in*: Mascle, A., Puigdefabregas, C., Luterbacher, H.P.,

- 992 and Fernandez, M., eds., Cenozoic Foreland Basins of Western Europe, Geological Society
993 Special Publications v. 134, p. 371-379.
- 994 Bornholdt, S., Nordlund, U., and Westphal, H., 1999, Inverse stratigraphic modeling using
995 genetic algorithms, *in*: Harbaugh, J.W., Watney, W.L., Rankey, E.C., Slingerland, R.,
996 Goldstein, R.H., and Franseen, E.K., eds., Numerical Experiments in Stratigraphy: Recent
997 Advances in Stratigraphic and Sedimentologic Computer Simulations,
998 doi:10.2110/pec.99.62.0085.
- 999 Braun, J., 2021, Comparing the transport-limited and ζ -q models for sediment transport, *Earth*
1000 *Surface Dynamics*, v. 10, p. 301-327, doi:10.5194/esurf-10-301-2022.
- 1001 Braun, J., Deschamps, F., Rouby, D., and Dauteuil, O., 2013, Flexure of the lithosphere and the
1002 geodynamical evolution of non-cylindrical rifted passive margins: Results from a
1003 numerical model incorporating variable elastic thickness, surface processes and 3D thermal
1004 subsidence, *Tectonophysics*, v. 604, p. 72—82, doi:10.1016/j.tecto.2012.09.033.
- 1005 Braun, J., Guillocheau, F., Robin, C., Baby, G., and Jelsma, H., 2014, Rapid erosion of the
1006 Southern African Plateau as it climbs over a mantle superswell, *Journal of Geophysical*
1007 *Research: Solid Earth*, v. 119, p. 6093—6112, doi:10.1002/2014JB010998.
- 1008 Burgess, P.M., Lammers, H., van Oosterhout, C., and Granjeon, D., 2006, Multivariate sequence
1009 stratigraphy: Tackling complexity and uncertainty with stratigraphic forward modeling,
1010 multiple scenarios, and conditional frequency maps, *American Association of Petroleum*
1011 *Geologists Bulletin*, v. 90, no. 12, p. 1883—1901, doi:10.1306/06260605081.
- 1012 Burgess, P.M., 2012, A brief review of developments in stratigraphic forward modelling 2000-
1013 2009, *in* Roberts, D.G. and Bally, A.W., eds., *Regional Geology and Tectonics: Principles*
1014 *of Geologic Analysis*, p. 378-404.

- 1015 Campforts, B., Shobe, C.M., Steer, P., Vanmaercke, M., Lague, D., and Braun, J., 2020,
1016 HyLands 1.0: a Hybrid Landscape evolution model to simulate the impact of landslides
1017 and landslide-derived sediment on landscape evolution, v. 13., p. 3863—3886,
1018 doi:10.5194/gmd-13-3863-2020.
- 1019 Carretier, S., Martinod, P., Reich, M., and Godderis, Y., 2016, Modelling sediment clasts
1020 transport during landscape evolution, *Earth Surface Dynamics*, v. 4, p. 237—251,
1021 doi:10.5194/esurf-4-237-2016.
- 1022 Cross, T.A. and Lessenger, M.A., 1999, Construction and application of a stratigraphic inverse
1023 model, *in*: Harbaugh, J.W., Watney, W.L., Rankey, E.C., Slingerland, R., Goldstein, R.H.,
1024 and Franseen, E.K., eds., *Numerical Experiments in Stratigraphy: Recent Advances in*
1025 *Stratigraphic and Sedimentologic Computer Simulations*, doi:10.2110/pec.99.62.0069.
- 1026 Dauteuil, O., Rouby, D., Braun, J., Guillocheau, F., and Deschamps, F., 2013, Post-breakup
1027 evolution of the Namibian margin: Constrains from numerical modeling, *Tectonophysics*,
1028 v. 604, p. 122—138, doi:10.1016/j.tecto.2013.03.034.
- 1029 Davy, P. and Lague, D., 2009, Fluvial erosion/transport equation of landscape evolution models
1030 revisited, *Journal of Geophysical Research*, v. 114, F03007, doi:10.1029/2008JF001146.
- 1031 DiBiase, R.A. and Whipple, K.X., 2011, The influence of erosion thresholds and runoff
1032 variability on the relationships among topography, climate, and erosion rate, *Journal of*
1033 *Geophysical Research*, v. 116, doi:10.1029/2011JF002095.
- 1034 Ding, X., Salles, T., Flament, N., Mallard, C., and Rey, P.F., 2019a, Drainage and sedimentary
1035 responses to dynamic topography, *Geophysical Research Letters*, v. 46, no. 24, p. 14385—
1036 14394, doi:10.1029/2019GL084400.

- 1037 Ding, X., Salles, T., Flament, N., and Rey, P., 2019b, Quantitative stratigraphic analysis in a
1038 source-to-sink numerical framework, *Geoscientific Model Development*, v. 12, p. 2571—
1039 2585, doi:10.5194/gmd-12-2571-2019.
- 1040 Doane, T.H., Furbish, D.J., Roering, J.J., Schumer, R., and Morgan, D.J., 2018, Nonlocal
1041 sediment transport on steep lateral moraines, Eastern Sierra Nevada, California, USA,
1042 *Journal of Geophysical Research: Earth Surface*, v. 123, no. 1, p. 187—208,
1043 doi:10.1002/2017JF004325.
- 1044 Falivene, O., Frascati, A., Gesbert, S., Pickens, J., Hsu, Y., and Rovira, A., 2014, Automatic
1045 calibration of stratigraphic forward models for predicting reservoir presence in exploration,
1046 *American Association of Petroleum Geologists Bulletin*, v. 98, no. 9, p. 1811-1835,
1047 doi:10.1306/02271413028.
- 1048 Falivene, O., Frascati, A., Bolla Pittaluga, M., and Martin, J., 2019, Three-dimensional reduced-
1049 complexity simulation of fluvio-deltaic clastic stratigraphy, *Journal of Sedimentary*
1050 *Research*, v. 89, p. 46-65, doi:10.2110/jsr.2018.73.
- 1051 Falivene, O., Prather, B.E., and Martin, J., 2020, Quantifying sand delivery to deep water during
1052 changing sea-level: Numerical models from the Quaternary Brazos Icehouse continental
1053 margin, *Basin Research*, v. 32, p. 1711-1733, doi:10.1111/bre.12449.
- 1054 Fofoula-Georgiou, E., Ganti, V., and Dietrich, W.E., 2010, A nonlocal theory of sediment
1055 transport on hillslopes, *Journal of Geophysical Research: Earth Surface*, v. 115, no. F2,
1056 doi:10.1029/2009JF001280.
- 1057 Furbish, D.J. and Roering, J.J., 2013, Sediment disentrainment and the concept of local versus
1058 nonlocal transport on hillslopes, *Journal of Geophysical Research: Earth Surface*, v. 118,
1059 no. 2, p. 937—952, doi:10.1002/jgrf.20071.

- 1060 Furbish, D.J., Roering, J.J., Doane, T.H., Roth, D.L., Williams, S.G., and Abbott, A.M., 2021,
1061 Rarefied particle motions on hillslopes—Part 1: Theory, *Earth Surface Dynamics*, v. 9, np.
1062 3, p. 539—576, doi:10.5194/esurf-9-539-2021.
- 1063 Granjeon, D. and Joseph, P., 1999, Concepts and applications of a 3-D multiple lithology,
1064 diffusive model in stratigraphic modeling, *in*: Harbaugh, J.W., Watney, W.L., Rankey,
1065 E.C., Slingerland, R., Goldstein, R.H., and Franseen, E.K., eds., *Numerical Experiments in*
1066 *Stratigraphy: Recent Advances in Stratigraphic and Sedimentologic Computer Simulations*,
1067 p. 197—210, doi:10.2110/pec.99.62.0197.
- 1068 Granjeon, D., 2014, 3D forward modelling of the impact of sediment transport and base level
1069 cycles on continental margins and incised valleys, *International Association of*
1070 *Sedimentology Special Publication*, v. 46, p. 453-472.
- 1071 Guerit, L., Yuan, X.P., Carretier, S., Bonnet, S., Rohais, S., Braun, J., and Rouby, D., 2019,
1072 Fluvial landscape evolution controlled by the sediment deposition coefficient: Estimation
1073 from experimental and natural landscapes, *Geology*, v. 47, no. 9, p. 853—856,
1074 doi:10.1130/G46356.1.
- 1075 Guillocheau, F., Rouby, D., Robin, C., Helm, C., Rolland, N., Le Carlier de Veslud, C., and
1076 Braun, J., 2012, Quantification and causes of the terrigenous sediment budget at the scale
1077 of a continental margin: a new method applied to the Namibia-South Africa margin, *Basin*
1078 *Research*, v. 24, p. 3—30, doi:10.1111/j.1365-2117.2011.00511.x.
- 1079 Harris, A.D., Covault, J.A., Madof, A.S., Sun, T., Sylvester, Z., and Granjeon, D., 2016, Three-
1080 dimensional numerical modeling of eustatic control on continental-margin sand
1081 distribution, *Journal of Sedimentary Research*, v. 86, p. 1434-1443,
1082 doi:10.2110/jsr.2016.85.

- 1083 Harris, A.D., Baumgartner, S.E., Sun, T., and Granjeon, D., 2018, A poor relationship between
1084 sea level and deep-water sand delivery, *Sedimentary Geology*, v. 370, p. 42-51,
1085 doi:10.1016/j.sedgeo.2018.04.002.
- 1086 Harris, A.D., Covault, J.A., Baumgartner, S., Sun, T., and Granjeon, D., 2020, Numerical
1087 modeling of icehouse and greenhouse sea-level changes on a continental margin: Sea-level
1088 modulation of deltaic avulsion processes, *Marine and Petroleum Geology*, v. 111, p. 807-
1089 814, doi:10.1016/j.marpetgeo.2019.08.055.
- 1090 Hereema, C.J. et al., 2020, What determines the downstream evolution of turbidity currents?
1091 *Earth and Planetary Science Letters*, v. 532, doi:10.1016/j.epsl.2019.116023.
- 1092 Hirsch, K.K., Schenck-Wenderoth, M., van Wees, J.-D., Kuhlmann, G., and Paton, D.A., 2010,
1093 Tectonic subsidence history and thermal evolution of the Orange Basin, *Marine and*
1094 *Petroleum Geology*, v. 27, p. 565—584, doi:10.1016/j.marpetgeo.2009.06.009.
- 1095 Hobley, D.E.J., Sinclair, H.D., Mudd, S.M., and Cowie, P.A., 2011, Field calibration of sediment
1096 flux dependent river incision, *Journal of Geophysical Research: Earth Surface*, v. 116, no.
1097 F4, doi:10.1029/2010JF001935.
- 1098 Imhof, M.G. and Sharma, A.K., 2006, Quantitative seismostratigraphic inversion of a prograding
1099 delta from seismic data, *Marine and Petroleum Geology*, v. 23, p. 735-744,
1100 doi:10.1016/j.marpetgeo.2006.04.004.
- 1101 Imhof, M.G. and Sharma, A.K., 2007, Seismostratigraphic inversion: Appraisal, ambiguity, and
1102 uncertainty, *Geophysics*, v. 72, no. 4, p. R51-R66, doi:10.1190/1.2720496.
- 1103 Jerolmack, D.J. and Paola, C., 2010, Shredding of environmental signals by sediment transport,
1104 *Geophysical Research Letters*, v. 37, no. 19, doi:10.1029/2010GL044638.

- 1105 Kaufman, P., Grotzinger, J.P., and McCormick, D.S., 1992, Depth-dependent diffusion algorithm
1106 for simulation of sedimentation in shallow marine depositional systems, *Kansas Geological*
1107 *Survey Bulletin*, v. 233, p. 489—508.
- 1108 Kenyon, P.M. and Turcotte, D.L., 1985, Morphology of a delta prograding by bulk sediment
1109 transport, *Geological Society of America Bulletin*, v. 96, no. 11, p. 1457—1465,
1110 doi:10.1130/0016-7606(1985)96<1457:MOADPB>2.0.CO;2.
- 1111 Klinger, E., Rickert, D., and Hasenauer, J., 2018, pyABC: distributed, likelihood-free inference,
1112 *Bioinformatics*, v. 34, no. 20, p. 3591—3593, doi:10.1093/bioinformatics/bty361.
- 1113 Kooi, H. and Beaumont, C., 1994, Escarpment evolution on high-elevation rifted margins:
1114 Insights derived from a surface processes model that combines diffusion, advection, and
1115 reaction, *Journal of Geophysical Research*, v. 99, no. 12, p. 12191—12209.
- 1116 Lessenger, M.A. and Cross, T.A., 1996, An inverse stratigraphic simulation model—is
1117 stratigraphic inversion possible? *Energy Exploration and Exploitation*, v. 14, no. 6, p.
1118 627—637, doi:10.1177/014459879601400606.
- 1119 Lowe, D.R., Grain flow and grain flow deposits, *Journal of Sedimentary Petrology*, v. 46, no. 1,
1120 p. 188—199.
- 1121 Luchi, R., Balachandar, S., Seminara, G., and Parker, G., 2018, Turbidity currents with
1122 equilibrium basal driving layers: A mechanism for long runout, *Geophysical Research*
1123 *Letters*, v. 45, no. 3, p. 1518—1526, doi:10.1002/2017GL075608.
- 1124 Martin, J., Paola, C., Abreu, V., Neal, J., and Sheets, B., 2009, Sequence stratigraphy of
1125 experimental strata under known conditions of differential subsidence and variable base
1126 level, *American Association of Petroleum Geologists Bulletin*, v. 93, no. 4, p. 503-533,
1127 doi:10.1306/12110808057.

- 1128 McKenzie, D., 1978, Some remarks on the development of sedimentary basins, *Earth and*
1129 *Planetary Science Letters*, v. 40, no. 1, p. 25—32, doi:10.1016/0012-821X(78)90071-7.
- 1130 Mohrig, D., Ellis, C., Parker, G., Whipple, K.X., and Hondzo, M., 1998, Hydroplaning of
1131 subaqueous debris flows, *Geological Society of America Bulletin*, v. 110, no. 3, p. 387—
1132 394, doi:10.1130/0016-7606(1998)110<0387:HOSDF>2.3.CO;2.
- 1133 Molnar, P., Brown, E.T., Burchfiel, B.C., Deng, Q., Feng, X., Li, J., Raisbeck, G.M., Shi, J.,
1134 Zhangming, W., Yiou, F., and You, H., 1994, Quaternary climate change and the
1135 formation of river terraces across growing anticlines on the north flank of the Tien Shan,
1136 China, *The Journal of Geology*, v. 102, no. 5, p. 583—602, doi:10.1086/629700.
- 1137 Moretti, I. and Turcotte, D.L., 1985, A model for erosion, sedimentation, and flexure with
1138 application to New Caledonia, *Journal of Geodynamics*, v. 3, no. 1—2, p. 155—168,
1139 doi:10.1016/0264-3707(85)90026-2.
- 1140 O'Malley, C.P.B., White, N.J., Stephenson, S.N., and Roberts, G.G., 2021, Large-scale tectonic
1141 forcing of the African Landscape, *Journal of Geophysical Research: Earth Surface*, v.
1142 126, doi:10.1029/2021JF006345.
- 1143 Niedoroda, A.W., Reed, C.W., Swift, D.J.P., Arato, H., and Hoyanagi, K., 1995, Modeling
1144 shore-normal large-scale coastal evolution, *Marine Geology*, v. 126, p. 181—199,
1145 doi:10.1016/0025-3227(95)98961-7.
- 1146 Paola, C., 2000, Quantitative models of sedimentary basin filling, *Sedimentology*, v. 47, no. s1,
1147 p. 121—178, doi:10.1046/j.1365-3091.2000.00006.x.
- 1148 Parker, G., Fukushima, Y., and Pantin, H.M., 1986, Self-accelerating turbidity currents, *Journal*
1149 *of Fluid Mechanics*, v. 171, p. 145—181, doi:10.1017/S0022112086001404.

- 1150 Paton, D.A., van der Spuy, D., di Primio, R., and Horsfield, B., 2008, Tectonically induced
1151 adjustment of passive-margin accommodation space: influence on the hydrocarbon
1152 potential of the Orange Basin, South Africa, *American Association of Petroleum*
1153 *Geologists Bulletin*, v. 92, no. 5, p. 589—609, doi:10.1306/12280707023.
- 1154 Pazzaglia, F.J. and Brandon, M.T., 1996, Macrogeomorphic evolution of the post-Triassic
1155 Appalachian mountains determined by deconvolution of the offshore basin sedimentary
1156 record, *Basin Research*, v. 8, no. 3, p. 255—278, doi:10.1046/j.1365-2117.1996.00274.x.
- 1157 Pirmez, C., Pratson, L.F., and Steckler, M.S., 1998, Clinoform development by advection-
1158 diffusion of suspended sediment: Modeling and comparison to natural systems, *Journal of*
1159 *Geophysical Research*, v. 103, no. B10, p. 24141—24157, doi:10.1029/98JB01516.
- 1160 Poag, C.W., 1992, U.S. Middle Atlantic continental rise: Provenance, dispersal, and deposition
1161 of Jurassic to Quaternary sediments, *in* Poag, C.W. and Graciansky, P.C., eds., *Geologic*
1162 *Evolution of Atlantic Continental Rises*: Springer, p. 100—156.
- 1163 Poag, C.W. and Sevon, W.D., 1989, A record of Appalachian denudation in postrift Mesozoic
1164 and Cenozoic sedimentary deposits of the U.S. Middle Atlantic continental margin,
1165 *Geomorphology*, v. 2, no. 1—3, p. 119—157, doi:10.1016/0169-555X(89)90009-3.
- 1166 Ramsay, P.J. and Cooper, J.A.G., 2002, Late Quaternary sea-level change in South Africa,
1167 *Quaternary Research*, v. 57, no. 1, p. 82—90, doi:10.1006/qres.2001.2290.
- 1168 Rivenaes, J.C., 1992, Application of a dual-lithology, depth-dependent diffusion equation in
1169 stratigraphic simulation, *Basin Research*, v. 4, p. 133—146, doi:10.1111/j.1365-
1170 2117.1992.tb00136.x.

- 1171 Rivenaes, J.C., 1997, Impact of sediment transport efficiency on large-scale sequence
1172 architecture: results from stratigraphic computer simulation, *Basin Research*, v. 9, p. 91—
1173 105, doi:10.1046/j.1365-2117.1997.00037.x.
- 1174 Roering, J.J., Kirchner, J.W., and Dietrich, W.E., 1999, Evidence for nonlinear, diffusive
1175 sediment transport on hillslopes and implications for landscape morphology, *Water*
1176 *Resources Research*, v. 35, no. 3, p. 853—870, doi:10.1029/1998WR900090.
- 1177 Ross, W.C., Halliwell, B.A., May, J.A., Watts, D.E., and Syvitski, J.P.M., 1994, Slope
1178 readjustment: A new model for the development of submarine fans and aprons, *Geology*,
1179 v. 22, p. 511—514, doi:10.1130/0091-7613(1994)022<0511:SRANMF>2.3.CO;2.
- 1180 Rouby, D., Bonnet, S., Guillocheau, F., Gallagher, K., Robin, C., Biancotto, F., Dauteuil, O., and
1181 Braun, J., 2009, Sediment supply to the Orange sedimentary system over the last 150 My:
1182 An evaluation from sedimentation/denudation balance, *Marine and Petroleum Geology*,
1183 v. 26, no. 6, p. 782-794, doi:10.1016/j.marpetgeo.2008.08.004.
- 1184 Rouby, D., Braun, J., Robin, C., Dauteuil, O., and Deschamps, F., 2013, Long-term stratigraphic
1185 evolution of Atlantic-type passive margins: A numerical approach of interactions
1186 between surface processes, flexural isostasy and 3D thermal subsidence, *Tectonophysics*,
1187 v. 604, p. 83—103, doi:10.1016/j.tecto.2013.02.003.
- 1188 Sadler, P.M., 1981, Sediment accumulation rates and the completeness of stratigraphic sections,
1189 *The Journal of Geology*, v. 89, no. 5, p. 569—584, doi:10.1086/628622.
- 1190 Salles, T., 2019, eSCAPE: Regional to global scale landscape evolution model v2.0,
1191 *Geoscientific Model Development*, v. 12, p. 4165—4184, doi:10.5194/gmd-12-4165-
1192 2019.

- 1193 Salles, T. and Hardiman, L., 2016, Badlands: An open-source, flexible and parallel framework to
1194 study landscape dynamics, *Computers & Geosciences*, v. 91, p. 77—89,
1195 doi:10.1016/j.cageo.2016.03.011.
- 1196 Salles, T., Ding, X., and Brocard, G., 2018, pyBadlands: A framework to simulate sediment
1197 transport, landscape dynamics and basin stratigraphic evolution through space and time,
1198 *PLoS ONE*, v. 13, no. 4, doi:10.1371/journal.pone.0195557.
- 1199 Schanz, S.A., Montgomery, D.R., Collins, B.D., and Duvall, A.R., 2018, Multiple paths to
1200 straths: A review and reassessment of terrace genesis, *Geomorphology*, v. 312, p. 12—
1201 23, doi:10.1016/j.geomorph.2018.03.028.
- 1202 Sclater, J.G. and Christie, P.A.F., 1980, Continental Stretching: An explanation of the Post-Mid-
1203 Cretaceous subsidence of the central North Sea Basin, *Journal of Geophysical Research:*
1204 *Solid Earth*, v. 85, no. B7, p. 3711—3739, doi:10.1029/JB085iB07p03711.
- 1205 Shobe, C.M., Tucker, G.E., and Barnhart, K.R., 2017, The SPACE 1.0 model: a Landlab
1206 component for 2-D calculation of sediment transport, bedrock erosion, and landscape
1207 evolution, *Geoscientific Model Development*, v. 10, no. 12, p. 4577—4604,
1208 doi:10.5194/gmd-10-4577-2017.
- 1209 Shobe, C.M., Braun, J., Yuan, X.P., Campforts, B., Gailleton, B., Baby, G., Guillocheau, F., and
1210 Robin, C., 2022, Code and data to accompany "Inverting passive margin stratigraphy for
1211 marine sediment transport dynamics over geologic time": Figshare data set, (available at
1212 <https://doi.org/10.6084/m9.figshare.20205077>).
- 1213 Sisson, S.A., Fan, Y., and Tanaka, M.M. (2007) Sequential Monte Carlo without likelihoods,
1214 *Proceedings of the National Academy of Sciences*, v. 104, no. 6, p. 1760-1765,
1215 doi:10.1073/pnas.0607208104.

- 1216 Sømme, T.O., Helland-Hansen, W., and Granjeon, D., 2009, Impact of eustatic amplitude
1217 variations on shelf morphology, sediment dispersal, and sequence stratigraphic
1218 interpretation: Icehouse versus greenhouse systems, *Geology*, v. 37, no. 7, p. 587-590,
1219 doi:10.1130/G25511A.1.
- 1220 Steckler, M.S., Reynolds, D.J., Coakley, B.J., Swift, B.A., and Jarrad, R., 1993, Modelling
1221 passive margin sequence stratigraphy, *in*: Posamentier, H.W., Summerhayes, C.P., Haq,
1222 B.U., and Allen, G.P., eds., *Sequence Stratigraphy and Facies Associations*, p. 19—41,
1223 doi:10.1002/9781444304015.ch2.
- 1224 Steckler, M.S., Swift, D.J.P., Syvitski, J.P., Goff, J.A., and Niedoroda, A.W., 1996, Modeling the
1225 sedimentology and stratigraphy of continental margins, *Oceanography*, v. 9, no. 3, p.
1226 183—188.
- 1227 Steckler, M.S., Watts, A.B., and Thorne, J.A., 1988, Subsidence and basin modeling at the U.S.
1228 Atlantic passive margin, *in*: Sheridan, R.E. and Grow, J.A., eds., *The Atlantic Continental*
1229 *Margin, U.S.: Geological Society of America, The Geology of North America*, v. 1—2, p.
1230 399—416..
- 1231 Stanley, J.R., Braun, J., Baby, G., Guillocheau, F., Robin, C., Flowers, R.M., Brown, R.,
1232 Wildman, M., and Beucher, R., Constraining plateau uplift in southern Africa by
1233 combining thermochronology, sediment flux, topography, and landscape evolution
1234 modeling, *Journal of Geophysical Research: Solid Earth*, v. 126, no. 7,
1235 doi:10.1029/2020JB021243.
- 1236 Straub, K.M., Duller, R.A., Foreman, B.Z., and Hajek, E.A., 2020, Buffered, incomplete, and
1237 shredded: The challenges of reading an imperfect stratigraphic record, *Journal of*
1238 *Geophysical Research: Earth Surface*, v. 125, no. 3, doi:10.1029/2019JF005079.

- 1239 Syvitski, J.P.M., Smith, J.N., Calabrese, E.A., and Boudreau, B.P., 1988, Basin sedimentation
1240 and the growth of prograding deltas, *Journal of Geophysical Research: Oceans*, v. 93, no.
1241 C6, p. 6895—6906, doi:10.1029/JC093iC06p06895.
- 1242 Syvitski, J.P.M. and Hutton, E.W.H., 2001, 2D SEDFLUX 1.0C:: an advance process-response
1243 numerical model for the fill of marine sedimentary basins, *Computers & Geosciences*, v.
1244 27, no. 6, p. 731—753, doi:10.1016/S0098-3004(00)00139-4.
- 1245 Talling, P.J., Summer, E.J., Masson, D.G., and Malgesini, G., 2012, Subaqueous sediment
1246 density flows: Depositional processes and deposit types, *Sedimentology*, v. 59, p. 1937—
1247 2003, doi:10.1111/j.1365-3091.2012.01353.x.
- 1248 Thran, A.C., East, M., Webster, J.M., Salles, T., and Petit, C., 2020, The influence of carbonate
1249 platforms on the geomorphological development of a mixed carbonate-siliciclastic margin
1250 (Great Barrier Reef, Australia), *Geochemistry, Geophysics, Geosystems*, v. 21,
1251 doi:10.1029/2020GC008915.
- 1252 Toni, T., Welch D., Strelkova, N., Ipsen, A., and Stumpf, M.P.H., 2009, Approximate Bayesian
1253 computation scheme for parameter inference and model selection in dynamical systems,
1254 *Journal of the Royal Society Interface*, v. 6, p. 187-202, doi:10.1098/rsif.2008.0172.
- 1255 Valla, P.G., van der Beek, P.A., and Lague, D., 2010, Fluvial incision into bedrock: Insights
1256 from morphometric analysis and numerical modeling of gorges incising glacial hanging
1257 valleys (Western Alps, France), *Journal of Geophysical Research: Earth Surface*, v. 115,
1258 no. F2, doi:10.1029/2008JF001079.
- 1259 Wynn, R.B., Weaver, P.P.E., Masson, D.G., and Stow, D.A.V., 2002, Turbidite depositional
1260 architecture across three interconnected deep-water basins on the north-west African
1261 Margin, *Sedimentology*, v. 49, no. 4, p. 669-695, doi:10.1046/j.1365-3091.2002.00471.x.

- 1262 Yanites, B.J., Becker, J.K., Madritsch, H., Schnellmann, M., and Ehlers, T.A., 2018, Lithologic
1263 effects on landscape response to base level changes: A modeling study in the context of the
1264 Eastern Jura Mountains, Switzerland, *Journal of Geophysical Research: Earth Surface*, v.
1265 122, p. 2196—2222, doi:10.1002/2016JF004101.
- 1266 Yuan, X.P., Braun, J., Guerit, L., Simon, B., Bovy, B., Rouby, D., Robin, C., and Jiao, R., 2019a,
1267 Linking continental erosion to marine sediment transport and deposition: A new implicit
1268 and $O(N)$ method for inverse analysis, *Earth and Planetary Science Letters*, v. 524,
1269 doi:10.1016/j.epsl.2019.115728.
- 1270 Yuan, X.P., Braun, J., Guerit, L., Rouby, D., and Cordonnier, G., 2019b, A new efficient method
1271 to solve the stream power law model taking into account sediment deposition, *Journal of*
1272 *Geophysical Research: Earth Surface*, v. 124, p. 1346—1365, doi:10.1029/2018JF004867.
- 1273 Yuan, X.P., Guerit, L., Braun, J., Rouby, D., and Shobe, C.M., 2022, Thickness of fluvial
1274 deposits records climate oscillations, *Journal of Geophysical Research: Solid Earth*, v. 127,
1275 no. 4, doi:10.1029/2021JB023510.
- 1276 Zhang, J., Sylvester, Z., and Covault, J., 2020, How do basin margins record long-term tectonic
1277 and climatic changes? *Geology*, v. 48, no. 9, p. 893—897, doi:10.1130/G47498.1.
- 1278 Zhang, J., Flaig, P., Wartes, M., Aschoff, J., and Shuster, M., 2021, Integrating stratigraphic
1279 modelling, inversion analysis, and shelf-margin records to guide provenance analysis: An
1280 example from the Cretaceous Colville Basin, Arctic Alaska, *Basin Research*, v. 33, no. 3,
1281 p. 1954-1966, doi:10.1111/bre.12543.